UNIVERSITAT POLITÈCNICA DE VALÈNCIA

_ TELECOM ESCUELA TÉCNICA VLC SUPERIOR DE INGENIERÍA DE TELECOMUNICACIÓN

# UNIVERSITAT POLITÈCNICA DE VALÈNCIA

## School of Telecommunications Engineering

# Optical switching in VO2/Si waveguides with efficient microheaters

End of Degree Project

Bachelor's Degree in Telecommunication Technologies and Services Engineering

AUTHOR: Morcillo Roldan, Juan Francisco

Tutor: Sanchis Kilders, Pablo

Experimental director: PARRA GOMEZ, JORGE

ACADEMIC YEAR: 2022/2023

## Resumen

Las redes neuronales artificiales se han erigido en los últimos años como una de las principales soluciones a la creciente demanda de transmisión y procesado de la información. En este contexto, los dispositivos fotónicos podrían ser determinantes, debido a sus bajas pérdidas y su bajo consumo, así como su gran velocidad de transmisión. La fotónica de silicio (Si) es una de las herramientas más atractivas por su compatibilidad con los semiconductores complementarios de óxido metálico (CMOS), que les confiere una gran escalabilidad y eficiencia en costes. Además, para conseguir las funcionalidades requeridas para las redes neuronales, los materiales compatibles con CMOS son esenciales, como puede ser el caso del dióxido de vanadio ($VO_2$), debido a sus propiedades de cambio de fase. En este trabajo se ha diseñado una guía híbrida de Si y $VO_2$, que actuará como un conmutador, mediante la excitación térmica de la transición de aislante a metálico del $VO_2$. El principal objetivo ha sido obtener las dimensiones y polarización óptimas de la guía híbrida. Además, se ha alcanzado la configuración térmica más eficiente para minimizar el consumo de potencia, así como el tiempo de conmutación.

## Resum

Les xarxes neuronals artificials s'han erigit en els últims anys com una de les principals solucions a la creixent demanda de transmissió i processament de la informació. En aquest context, els dispositius fotònics podrien ser determinants, a causa de les seues baixes pèrdues i el seu baix consum, així com la seua gran velocitat de transmissió. La fotònica de silici (Si) és una de les solucions més atractives per la seua compatibilitat amb els semiconductors complementaris d'òxid metàl·lic (CMOS), que els confereix una gran escalabilitat i eficiència en costos. A més, per a aconseguir les funcionalitats requerides per a les xarxes neuronals, els materials compatibles amb CMOS són essencials, com pot ser el cas del diòxid de vanadi ($VO_2$), a causa de les seues propietats de canvi de fase. En aquest treball s'ha dissenyat una guia híbrida de Si i $VO_2$, que actuarà com un commutador, mitjançant l'excitació tèrmica de la transició d'aïllant a metàl·lic del $VO_2$. El principal objectiu ha sigut obtindre les dimensions i polarització òptimes de la guia híbrida. A més, s'ha aconseguit la configuració tèrmica més eficient per a minimitzar el consum de potència, així com el temps de conmutació.

## Abstract

Artificial neural networks (ANNs) have emerged in the recent years as a solution to the increasing demand for information transmission and processing. In this context, photonic hardware may play a leading role, given their inherent low losses and low energy consumption, as well as their fast speed. Silicon (Si) photonics are one of the most attractive solutions in this field because of their complementary metal-oxide-semiconductor (CMOS) compatibility, which allows a great scalability and cost-effectiveness. Besides, in order to enable ANN functionalities, CMOS-compatible materials such as vanadium dioxide ($VO_2$) play an essential role given, in this case, its phase change properties. In this project, a hybrid $VO_2$/Si waveguide has been designed with the main goal of achieving a switching device, by means of thermally exploiting the $VO_2$ insulator-to-metal (IMT) transition. Designing the optimal dimensions of the hybrid waveguide, as well as the best polarization has been the main goal of this project. Furthermore, the most efficient heating configuration has been attained in order to minimize power consumption and switching time.

# Table of contents

# Chapter 1. Introduction

## 1.1 Motivation

### *1.1.1 Silicon PICs and heterogeneous integration*

Nowadays, telecommunications have reached their highest toll in history, and they are rising every single day. Therefore, there is a huge need for storing and distributing information in order to keep all the users connected. This requires a large number of electronic devices. Electronic devices represent the bottleneck of current telecommunications since they are limited to transmission speeds of Gb/s [1]. Besides, electronic devices also produce large amounts of thermal energy due to the Joule effect. Cooling down these devices is then necessary, and this process represents a high energy consumption. Data centres used in telecommunications account right now for about 1% of the total energy consumption in the world [2].

On the other hand, photonic integrated circuits (PICs) are based on the transmission of light. Light transmission leads to bandwidths several orders of magnitude higher. Then, circuits based on its transmission are capable to be many times more efficient (Tb/s) than electrical circuits. And lastly, thermal effects in optical circuits are much lower than in electronic ones, leading to much lower energy consumptions.

Amongst all the possible materials that can be used to design these PICs, in this project we will focus mainly on those made up of silicon. Silicon presents a high refractive index (n = 3.47) at telecom C-band wavelength (λ = 1550 nm). Thus, silicon PICs are able to confine light in strongly reduced spaces in the order of micrometres. This feature makes them very attractive in the design of larger devices because of their small footprint and, therefore, their scalability. However, the most important feature of silicon PICs is their compatibility with fabrication processes based on complementary metal-oxide semiconductors (CMOS) [3]. CMOS devices are widely used in the nano electronics industry. Therefore, their compatibility enables the possibility of creating electronic-photonic systems that are also monolithic. This means that both photonic and electronic circuits can be set up in one sole substrate or chip, which also reinforces their low footprint and scalability.

However, Si PICs are not the most suitable for creating active devices. While Si waveguides (intrinsically passive) are widely popularised, active Si devices cannot reach such levels. Active devices can modify the properties of the propagated modes. For that matter, it is needed to exploit whether a phase or amplitude change of the mode. To achieve this, a wide variation in the refractive index or the extinction coefficient, respectively, is necessary. The rationale for this statement can be derived from the general solution for the wave equation is shown next (1.1):

$$E(x,y,z,t) = E(x,y)e^{-\alpha z}e^{-j\beta z}e^{j\omega t} \tag{1.1}$$

where E(x,y) is the field distribution of the propagated mode, α stands for the propagation losses (amplitude), β is the phase term and ω is the angular frequency associated to time evolution. If we consider the steady-state, we obtain the following equation (1.2):

$$E(x,y,z) = E(x,y)e^{-\alpha z}e^{-j\beta z} \tag{1.2}$$

where:

$$\alpha = \frac{2\pi}{\lambda}\kappa_{eff} \tag{1.3}$$

$$\beta = \frac{2\pi}{\lambda}n_{eff} \tag{1.4}$$

The parameters $n_{eff}$ and $k_{eff}$ stand for the effective index of the propagated mode. Its value depends on the waveguide geometry and materials, the polarization and the wavelength. These are the parameters which will be analysed in this project. So, for a given λ and z, a wider variation on $k_{eff}$ and $n_{eff}$ will lead to higher changes in amplitude and phase, creating more efficient and compact active devices.

Therefore, in order to fabricate more efficient active devices, it is needed to introduce materials which present a high index change that can be triggered by some way. Among the different families of advanced materials, phase-change materials (PCMs) stand out for their unique electro-optical properties. PCMs feature a transition between two states or phases, and they present a different refractive index in each of the states. We will focus mainly on $VO_2$, though there are other vanadium oxides such as VO, $V_2O_3$, etc. There are also chalcogenides compounds used mainly for rewriteable data storage [4].

### *1.1.2 Optical properties of $VO_2$*

As it was stated in the previous section, PCMs are attractive for building efficient photonic active devices. $VO_2$ can be presented in two different states that are metallic (rutile phase) and insulating (monoclinic phase). Then, $VO_2$ plays a big role in the PCMs family, given its metal-insulator transition (MIT) or insulator-metal transition (IMT). The only difference in this nomenclature is which state takes place the first. However, in order to attain this transition, there are many possible stimuli that can be triggered in the $VO_2$ such as external heating, carrier injection or light. In this project, we will thermally trigger the MIT using external heating by means of a microheater. In Fig. 1.1 it can be seen the whole spectrum of different stimuli that have been demonstrated to trigger this transition.

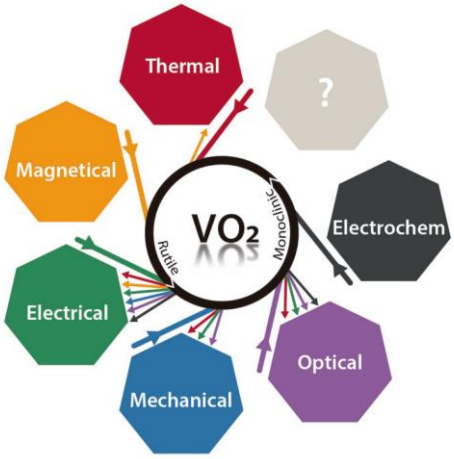


**Figure 1.1.** Different stimuli used to achieve the MIT. The '?' block represents inputs/outputs to be discovered [5].

Besides, one of the most interesting features of this material is that a low temperature is needed to thermally trigger this IMT response. $VO_2$ phase transition occurs moderately near room temperature at around 65ºC (338K), while other oxides may need higher temperatures to achieve this transition, as it can be seen in Fig. 1.2:

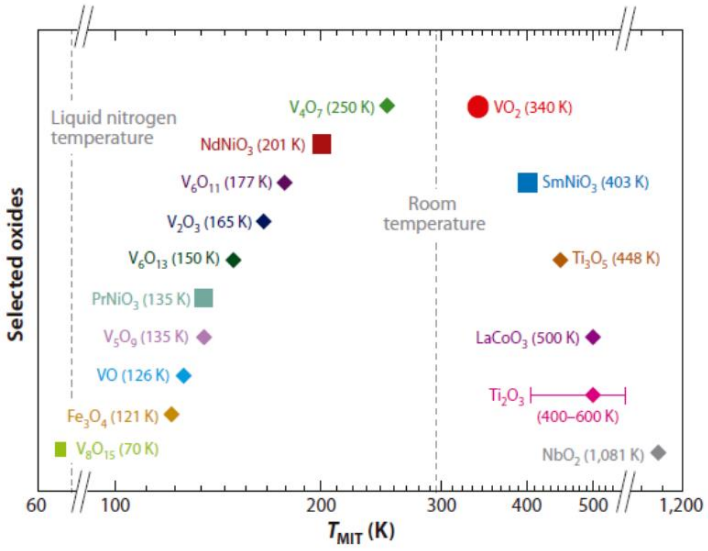


**Figure 1.2.** Needed temperature in order to achieve the MIT ($T_{MIT}$) for a series of oxides [6].

Also, another remarkable point in the MIT that takes place in the $VO_2$ is that this process is hysteretic. The hysteresis loop means that the transition from one phase to another does not occur at the same temperature; while the IMT temperature is 65ºC, the MIT temperature is around 40ºC (see Fig. 1.3). The hysteresis loop can be exploited for designing chips with bistable response, and thereby build optical devices with memory. [7].

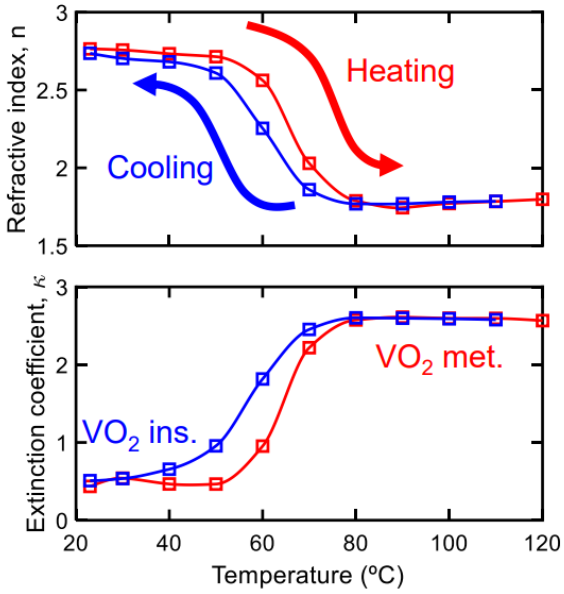


**Figure 1.3.** Refractive index (n) and extinction coefficient (k) for $VO_2$ depending on the temperature [8].

Lastly, but most importantly, the main difference between metallic and insulating states relies on their refractive indices. This can also be seen in Fig. 1.3, while for insulating $VO_2$, $n + ki = 2.756 + 0.451i$, and for the metallic $VO_2$, $n + ki = 1.788 + 2.574i$. When designing an optical switch, we will only focus on the amplitude change, this is, the amount of propagation losses introduced. Therefore, for this project, we will mainly exploit the dramatic variation in the extinction coefficient.

### *1.1.3 Optical switching role in photonic neural networks*

Optical switching is useful for several applications such as optical communications, datacom [1], space communications [9] and LiDAR [10], to name a few. Amongst these several applications, optical switching is being exploited recently in artificial neural networks (ANNs). ANNs mimic the way our brains process the information they receive. ANNs consist of a very large number of differenced units that work independently but towards a common goal. These units are the neurons. Every neuron processes the received information and sends it to the next one. Thus, an artificial system consisting of many layers of neurons is created.

Besides, every artificial neuron is made up of several parts that play a role so as to process the information and send it to the next neuron. The information is received in the form of many input signals. A simplified scheme of an artificial neuron is shown below (see Fig. 1.4):

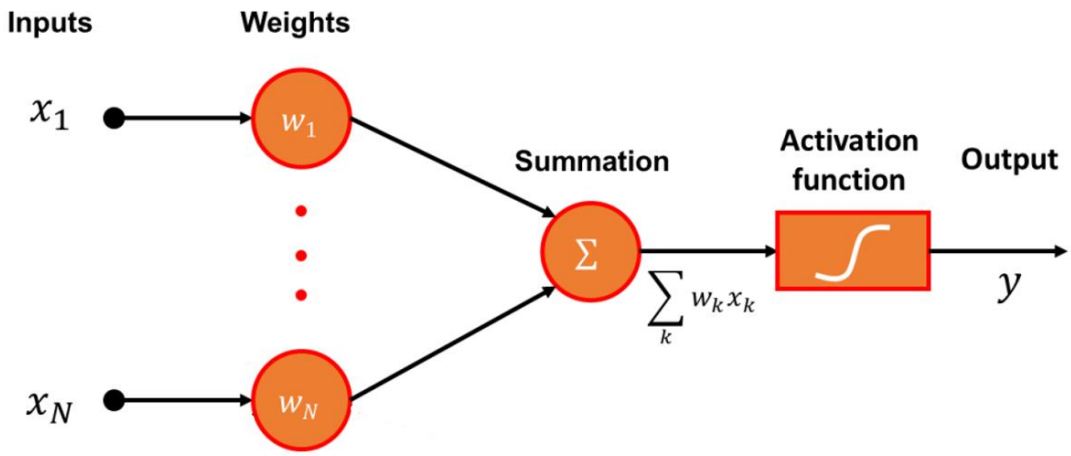


**Figure 1.4.** Structure of an artificial neuron.

The first step that takes place inside the neuron structure is to assign a weight to every input, since not all of them are equally important in the processing of the information. Then, all the weighted input signals are added up. This building block is the weighted summation. Afterwards, the summated signal is introduced into a non-linear activation function that prevents the output signal from exceeding a given amplitude for the next neuron[11]. After travelling through the activation function, the signal is then sent to the next layer of neurons in order to repeat the process again. Summarizing, there are two principal building blocks in the structure of a neuron: the weighted summation and the activation function.

In this line of work, photonics can play a big role given their inherent low propagation losses and fast speed [12]. ANNs can take advantage of the CMOS-compatibility presented by the silicon photonics in order to attain scalable and cost-effective devices [13]. The optical switch we are

going to design in the present project consists of a hybrid $VO_2$/Si waveguide that can be leveraged to act as the two building blocks of the neuron scheme described earlier.

On the one hand, the multilevel plasticity of the optical switch can be used to implement the weighting function of the neurons. This is, by varying the level of losses attained after travelling through the waveguide, we can assign each level to the weight of the input, e.g., in the low loss state, $w_k = 1$, but if the losses are maximal, $w_k = 0$. The multilevel plasticity means that each one of the in-between levels can also be achieved, thus generating an analogic representation of all the weights of the neuron.

On the other hand, a hybrid $VO_2$/Si waveguide can be leveraged to attain the clipped rectified linear unit (ReLu) activation function (see Fig. 1.5). ReLu and clipped ReLu are just two of many activation functions that are used in ANNs. ReLu transforms the negative input values to zero, while maintaining the positive values unaltered. The clipped ReLu is equal to the ReLu function but with the sole difference that when a given threshold is reached, the response enters a saturation zone. To achieve how the designed waveguide can implement this activation function, we must explain the optical limiting condition. The optical limiting condition states that when the induced losses in the waveguide match the increment in the input power, the output power in the waveguide will not increase with this increment; it will enter a constant regime [14]. Thus, when the optical pulse is introduced in the waveguide, the $VO_2$ patch placed on top will increase its temperature producing an all-optical switching, therefore inducing additional losses on the waveguide, and causing the optical limiting condition to be achieved.

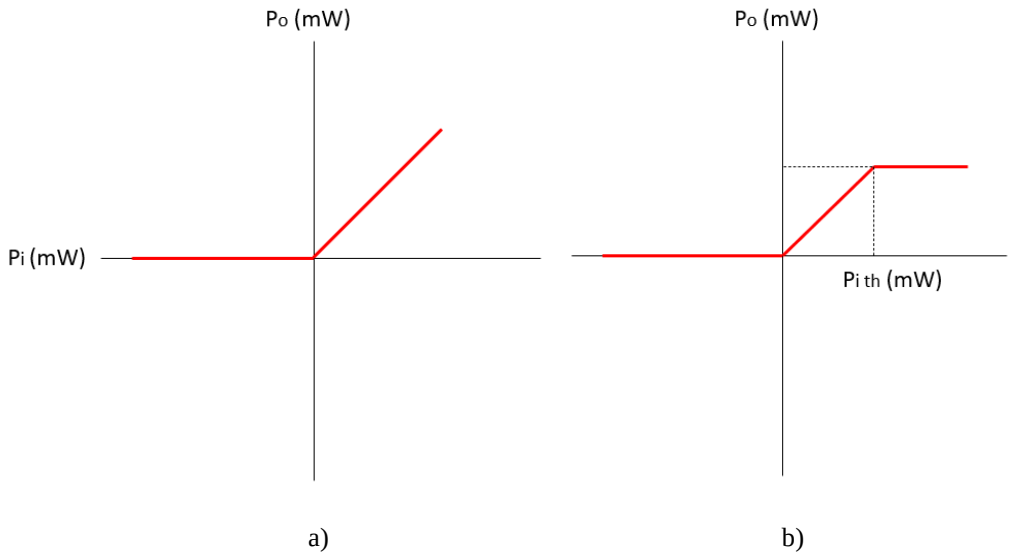


**Figure 1.5.** ReLu (a) and clipped ReLu (b) responses. 'th' marks the threshold at which the response starts saturating.

## 1.2 Objectives

The objective of this project is to design an optical switching device consisting of a hybrid $VO_2$/Si waveguide. Such waveguide will act as a switch by varying the state of the $VO_2$ layer placed on top of the silicon. The $VO_2$ variation will be triggered thermally using a Ti heater.

Therefore, the specific objectives of this project are:

- To determine via numerical simulation the optimal dimensions of the $VO_2$ layer and the best mode polarization in order to minimize losses and achieve a robust design against manufacturing imprecisions.
- To design the optimal Ti heater configuration to minimize power consumption and maximize the efficiency of the device.
- To physically implement the hybrid waveguide in the lab and analyse the attained losses using the lab equipment.

## 1.3 Methodology

In order to fulfil our objectives, the work will be mainly divided into three steps. Firstly, the dimensions of the hybrid waveguide will be established by using numerical simulations of the modes, trying to minimize the losses. For that matter, we will use the finite elements simulator FemSIM contained in RSoft. FemSIM calculates the effective indices of every one of the modes simulated. Then, these values will be processed using MATLAB to find the associated insertion losses. FemSIM also presents a sweep tool called MOST Scan. This tool allows us to vary the parameters of the design within a given range. We will use MOST Scan to find the thickness and length of the $VO_2$ layer that minimize the insertion losses and create the most robust device.

These results will then be verified using a Finite Difference Time Domain (3D-FDTD) simulator also contained in RSoft. This simulator will allow us to take into account all the losses produced in the waveguide, not only the insertion losses, but also the coupling losses. This simulation will be used to verify the optical response of the hybrid waveguide. If necessary, a redesign of the structure may be done.

The third and last step is to calculate the minimal power consumption of the Ti heater that allows the $VO_2$ layer to achieve its transition temperature. For that, we will use the physics simulation software COMSOL Multiphysics. COMSOL will allow us to perform heat propagation simulations and find out what is the minimal power that needs to be injected in the heater. Besides, the Ti heater will need to be placed at a minimum distance from the hybrid waveguide in order to avoid extra optical losses. This distance or gap will be found using the FemSIM simulator once again.

In addition to the simulated work, this project will also contain a preliminary experimental characterization of the targeted optimal design. For this matter, the fabrication mask will also be designed, and the characterization will take place in a laboratory, making use of a photonic chips setup.

The temporal distribution of the different tasks that have been performed in the development of this project can be seen in the following Gantt chart (see Fig. 1.6):

| | January | February | March | April | May | June | July |
|---|---|---|---|---|---|---|---|
| $VO_2$/Si technology review | | | | | | | |
| Optical analysis | | | | | | | |
| Thermal analysis | | | | | | | |
| Experimental characterization | | | | | | | |
| Data processing | | | | | | | |
| Report document | | | | | | | |

**Figure 1.6.** Gantt diagram showing the temporal distribution of the tasks.

## 1.4 Contribution to the SDGs

PICs can be leveraged to obtain ultra-compact and low loss photonic devices. As it was stated in the previous sections, a hybrid $VO_2$/Si waveguide will be optimized in order to attain the best performance at the lowest level of energy consumption.

Therefore, technological advances in the field of PICs such as this hybrid waveguide can be directly associated with the fulfilment of the Sustainable Development Goal (SDG) number 9: Industry, innovation and infrastructure, since this device could lead to building resilient infrastructure and a sustainable industrialization.

# Chapter 2. Performance analysis of the $VO_2$/Si waveguide

## 2.1 Description of waveguide structure and material properties

During the entire project, the waveguide structure that will be considered consists of a Si waveguide, which is surrounded by $SiO_2$. The waveguide used is a standard 220x500-nm-section guide (Figs. 2.1 and 2.2). Besides, the main highlight of the project is the influence of a $VO_2$ layer, whose temperature will vary in order to achieve the desired state commutation from insulating to metallic state. The $VO_2$ layer will be placed on top and sides of the Si waveguide.

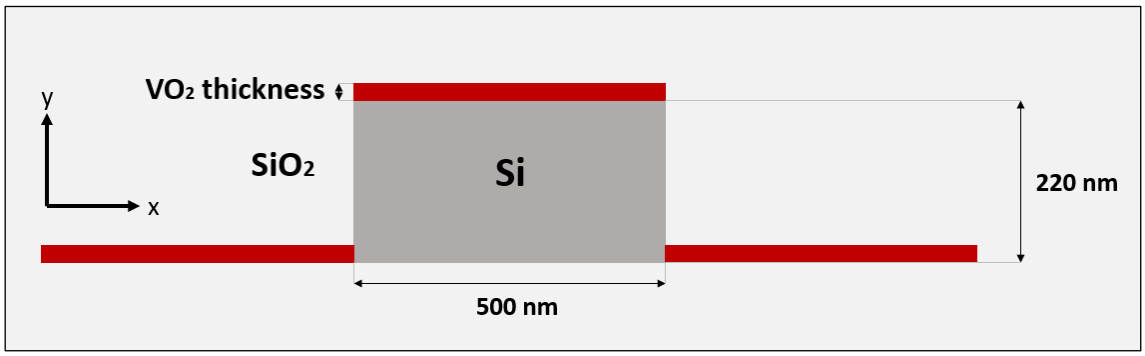


**Figure 2.1.** Cross-section and dimensions of the $VO_2$/Si waveguide.

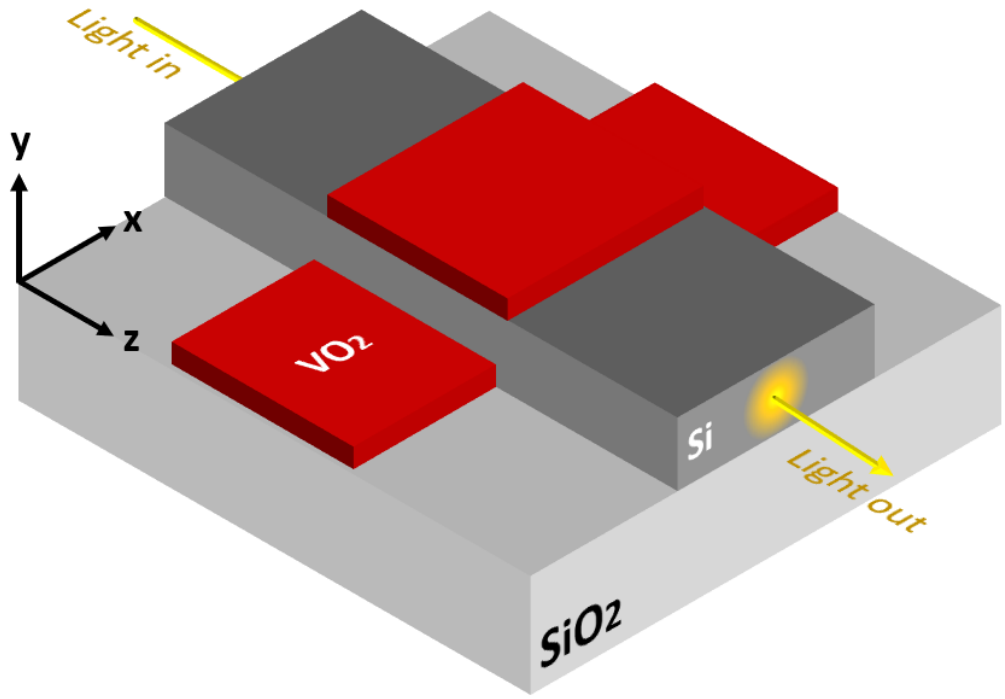


**Figure 2.2.** 3D representation of the waveguide structure.

As mentioned before, the main goal of the project is to create a waveguide that can switch from a light-transmitting state into a light-absorbing one. $VO_2$ plays a determinant role so as to achieve

this. When the $VO_2$ layer placed on top of the waveguide is found on its insulating state, light will be able to propagate throughout the waveguide. On the contrary, if $VO_2$ changes to the metallic state, the absorption of light will increase dramatically. This turns the waveguide into a switch that can be activated via external heating.

Such a variation in the absorption of the $VO_2$ between the metallic and insulating states dwells on the large difference of the refractive index between both states. The $VO_2$ refractive index considered for this work is, for the insulating $VO_2$ (i-$VO_2$) = 2.756 + 0.451i, and for the metallic $VO_2$ (m-$VO_2$) = 1.788 + 2.574i. All the considered refractive indices can be seen in the following Table 2.1:

| **i-$VO_2$** | **m-$VO_2$** | **$SiO_2$** | **Si** | **Ti** |
|---|---|---|---|---|
| 2.756 + 0.451i [8] | 1.788 + 2.574i [8] | 1.444 [15] | 3.476 [16] | 3.680 + 4.610i [17] |

**Table 2.1.** Refractive indices at λ = 1550 nm for the materials used.

In this work, we will focus on the telecom C-band. Therefore, all the following calculations have been performed taking into account a central wavelength of λ = 1550 nm.

## 2.2 Analysis of $VO_2$ thickness

### *2.2.1 Analysis of the effective indices of TE and TM modes.*

Once the waveguide design has been stablished and the $VO_2$ optical properties have been briefly explained, the first step in order to find the optimal switching device will be to discern what should be the thickness of the $VO_2$ layer placed on top of the waveguide. For that matter, we will consider a range of thicknesses varying from 0 to 100 nm, which is a range value typically used in the literature [13]. The simulation sweep will be performed using the software RSoft. RSoft is a software designed to perform photonic simulations. More specifically, we will be using its FemSIM tool. FemSIM allows us to calculate the effective indices of the several modes that propagate throughout a waveguide, analysing them in a section of said guide. This sweep will be carried out for both states of the $VO_2$ layer (i-$VO_2$ and m-$VO_2$) and initially, not only the upper layer will be state switched, but also the layers on the sides of the waveguide. As said before, the only practical difference we will consider between the states will be the refractive indices introduced in the material properties defined in RSoft. In the following Fig. 2.3, we can observe the refractive indices in the cross-section of the hybrid waveguide. These indices will be used by FemSIM to calculate the effective indices of the modes.

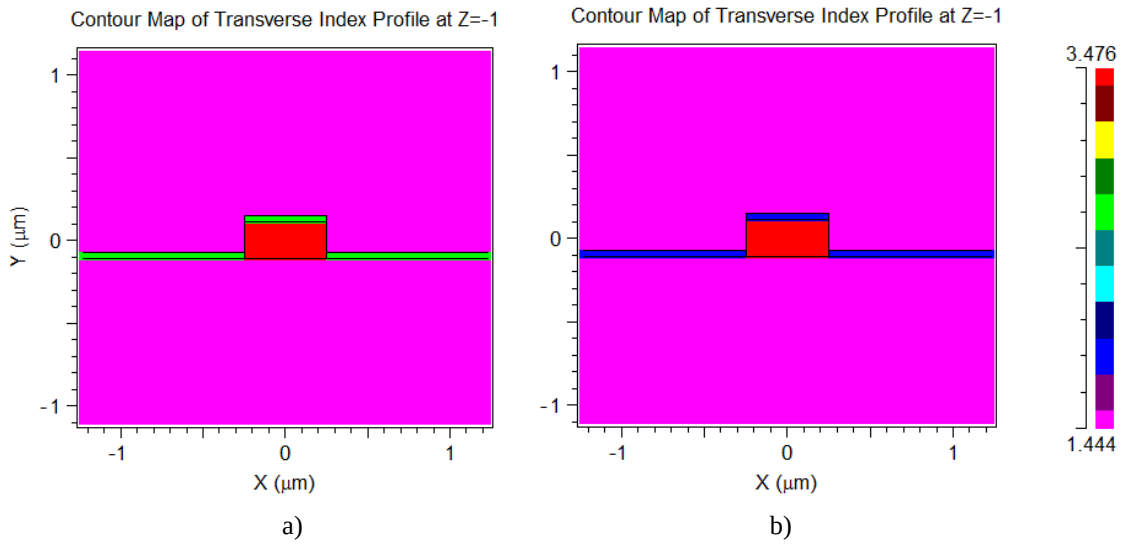


**Figure 2.3.** Cross-section of the refractive indices for a) i-$VO_2$ layer and b) m-$VO_2$ layer.

The next step in the simulation is to define a mesh. This mesh is a division of the whole simulation region and consists of every one of the points where the Maxwell equations are going to be numerically solved. There is a trade-off between accuracy and computational cost. In this regard, since it is not needed the same accuracy in all the simulation region, we will use a non-uniform grid with finer resolution in the regions the optical mode will be confined such as the $VO_2$ layer and Si core, and a more coarse grid in the surroundings. The non-uniform mesh can be visualized in the following Fig. 2.4:

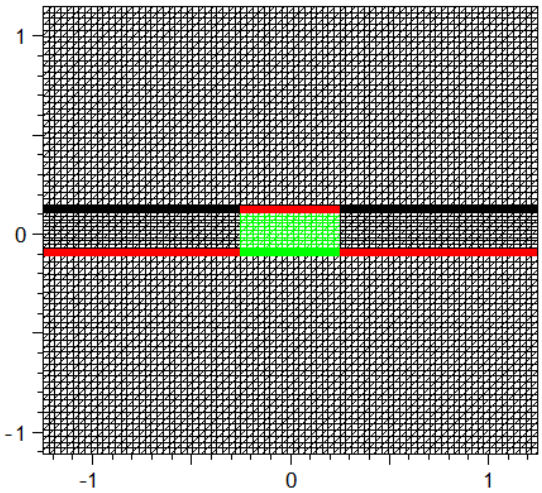

**Figure 2.4.** Non-uniform mesh used for FemSIM to numerically solve the mode equations.

Once the main parameters for the simulations have been defined, we will carry out a sweep for all of the simulations. This will be done using the MOST Scan tool of RSoft. This feature allows to subsequently perform several simulations varying one or more parameters. In this case, as it was stated, the $VO_2$ layer thickness will vary from using no layer to 100 nm thickness, with an increasing step of 5nm. In the next Fig. 2.5, we can see the fundamental transverse electric (TE)

and transverse magnetic (TM) modes of the silicon waveguide without $VO_2$, so we are then able to analyse the effects of introducing the layer.

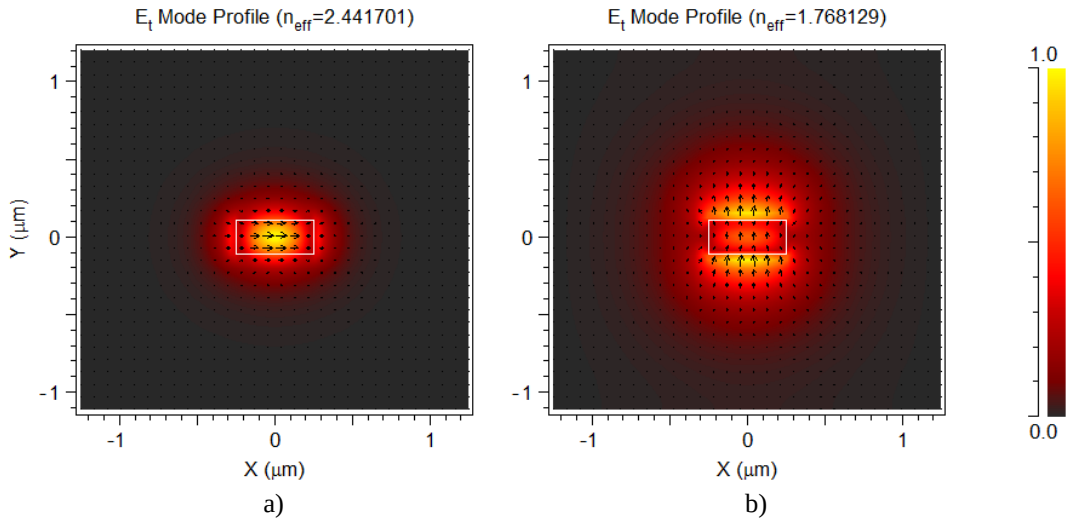


**Figure 2.5.** Fundamental modes when no $VO_2$ layer is used: a) TE and b) TM. The arrows stand for the direction of the E field.

In the following Fig. 2.6, we can see an example of the fundamental modes TE and TM for both states of the $VO_2$ layer. In this example, the selected $VO_2$ thickness is 40 nm.

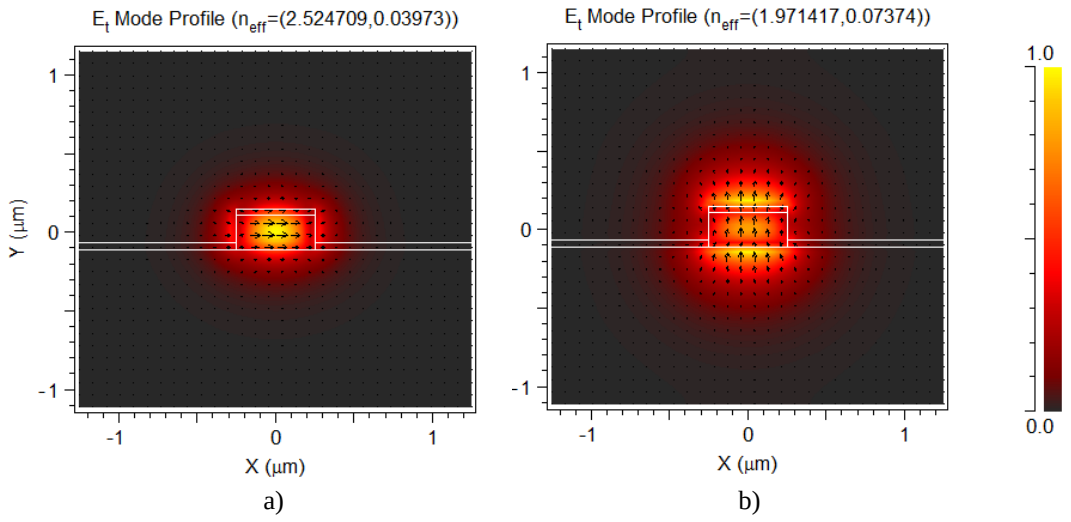

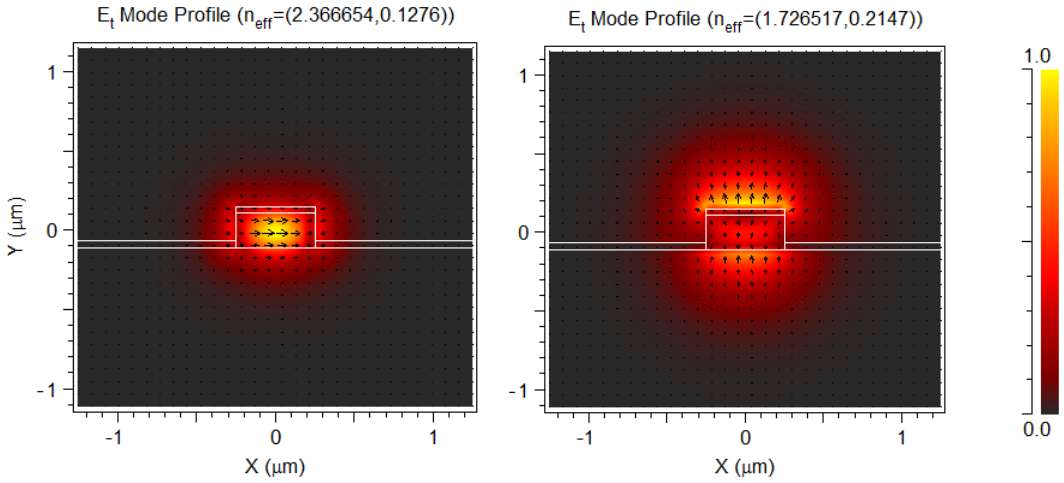


c) d)

**Figure 2.6.** Fundamental modes: a) i-$VO_2$ TE, b) i-$VO_2$ TM, c) m-$VO_2$ TE and d) m-$VO_2$ TM.

After all the simulations have been carried out, the values for the effective indices of the fundamental TE and TM modes have been processed using the software MATLAB and in the following graphs (see Fig. 2.7) we can see the real part for the effective indices.

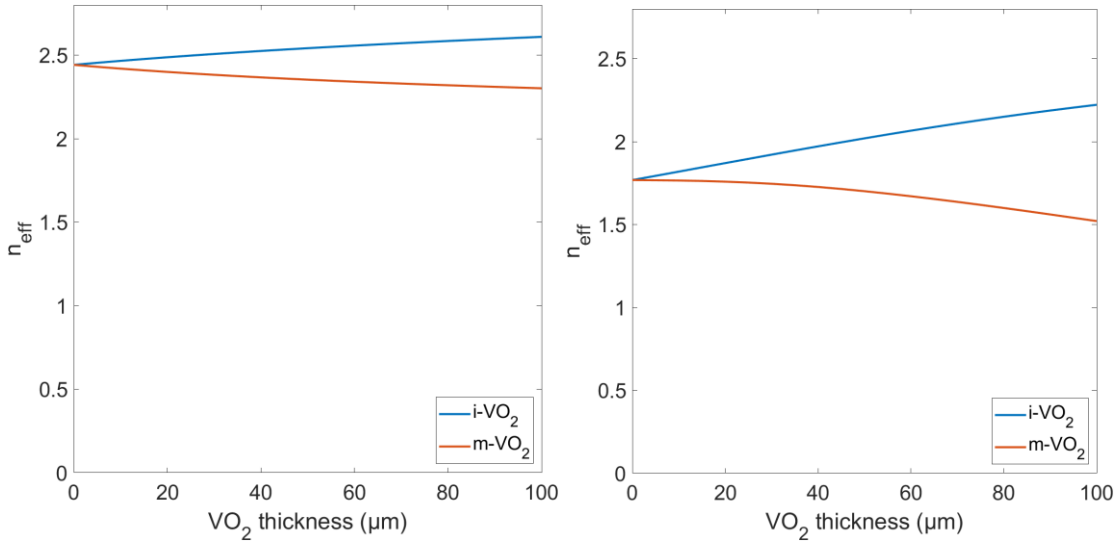


a) b)

**Figure 2.7.** Real part of effective indices for: a) fundamental TE mode. b) fundamental TM mode.

In the aforementioned graphs we can see how the values of both the effective indices increase with the thickness of the i-$VO_2$ layer. This is because the real part of the i-$VO_2$ index (see Table 2.1) is high in relation to the Si index. Meanwhile, in the case of the m-$VO_2$, the real effective index decreases as the thickness increases. This is also due to the fact that m-$VO_2$ real index is lower than i-$VO_2$ one.

TE fundamental mode indices are higher than TM fundamental mode ones, because there is a higher interaction with the $VO_2$ in the TM mode due to its nature (see Fig. 2.6), and therefore decreasing the effective index, since $VO_2$ index (real part) is lower than Si index in both cases.

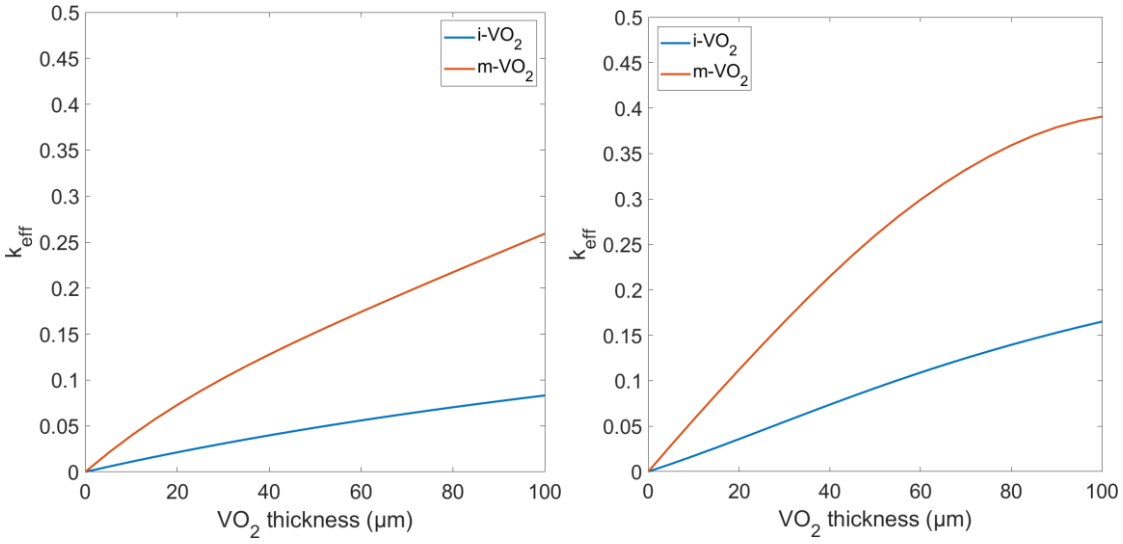


a) b)

**Figure 2.8.** Imaginary effective indices for: a) fundamental TE mode. b) fundamental TM mode.

In both TE and TM modes, it can easily be seen that $k_{eff}$, and therefore, propagation losses, increase when the $VO_2$ layer thickness increases (see Fig. 2.8).

On the other hand, it can also be seen that in the m-$VO_2$ case, $k_{eff}$ is higher than in i-$VO_2$, meaning that there will be more losses in the metallic case, as it was expected.

Also, $k_{eff}$ is higher in the TM fundamental mode than in the TE fundamental mode. This will result in higher propagation losses in the TM mode, and it is due to a higher interaction with the top $VO_2$ layer of this mode.

### *2.2.2 Analysis of propagation losses*

Once the effective indices have been calculated for both $VO_2$ states, it is possible to find the propagation losses (α) for each of the modes TE and TM. It is known, using equation 1.3, that the value (in dB/μm) for the propagation losses can be found using the following equation (2.1):

$$\alpha\left(\frac{dB}{\mu m}\right) = 20log_{10}(e)\frac{2\pi}{\lambda}\kappa_{eff} \tag{2.1}$$

In the following graphs we can observe how these propagation losses vary with the $VO_2$ thickness for i-$VO_2$ and m-$VO_2$ respectively (see Fig. 2.9):

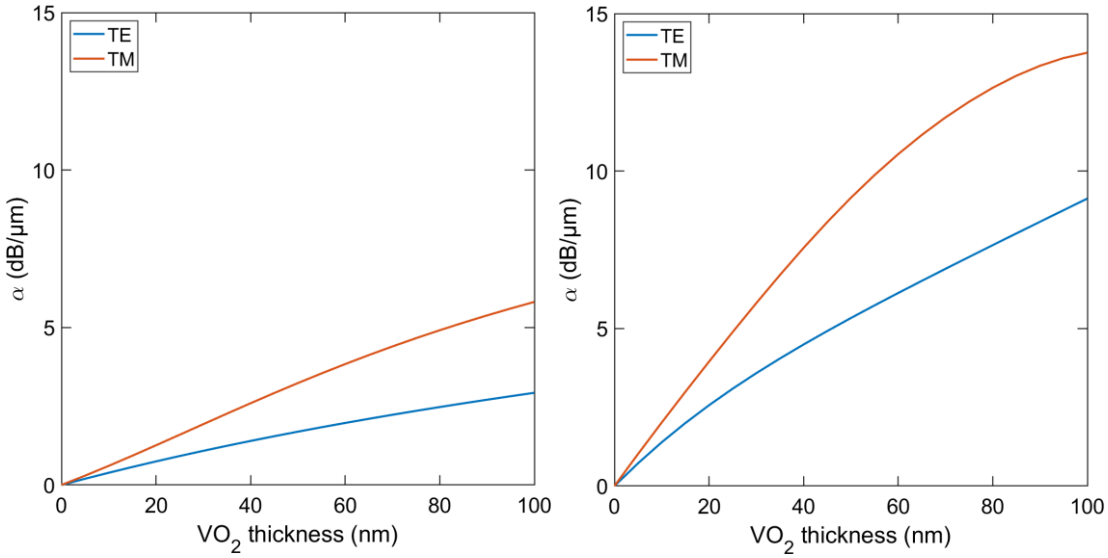


**Figure 2.9.** Propagation losses (dB/μm) for: a) i-$VO_2$ layer and b) m-$VO_2$ layer.

As it was expected, propagation losses reach considerably higher levels for m-$VO_2$ than they do for i-$VO_2$. This is due to the fact that was stated previously: the imaginary effective indices for the first state present higher values than those for the latter one.

Besides, propagation losses are higher for the TM fundamental mode than for the TE one, as it was previously predicted.

Nonetheless, these propagation losses depend on the length of the $VO_2$ layer as well, so they can widely vary with dependence of the selected length.

## 2.3 Analysis of optical switching

The main goal of Chapter 2 is to define the optimal structure of the hybrid $VO_2$/Si waveguide. Therefore, we will now find the adequate length and thickness of the $VO_2$ patch placed on top of the waveguide.

Now that the propagation losses have been calculated for both $VO_2$ states and both propagated modes, the next step is to analyse what would the effect of switching from one state to another be on the insertion losses (IL) and the extinction ratio (ER), both in units per length. When those two parameters are obtained, we will be able to determine the optimal $VO_2$ length and thickness for a given extinction ratio value.

### *2.3.1 Analysis of IL and ER (units per length) for TE and TM*

Insertion losses are a measure of the difference between the power that is injected into the waveguide and the actual power that succeeds to be transmitted throughout it. Such optical losses come mainly from absorption (propagation losses) and coupling mismatch (coupling losses). On the other hand, the extinction ratio is defined as the losses relation obtained when switching from one $VO_2$ state to another.

According to this information, insertion losses will be selected amongst the propagation losses of both states, as the lowest of the two values (2.2). Looking at graphs in Figure 2.8, it can be stated that those lowest losses can be found on the insulating $VO_2$ for polarizations TE and TM.

$$IL\left(\frac{dB}{\mu m}\right) = min\left(\alpha_{i-VO_2}, \alpha_{m-VO_2}\right) \tag{2.2}$$

Therefore, the insertion losses we will consider are basically the propagation losses that we previously calculated for i-$VO_2$ and can also be examined in the upcoming graph (see Fig. 2.10.a):

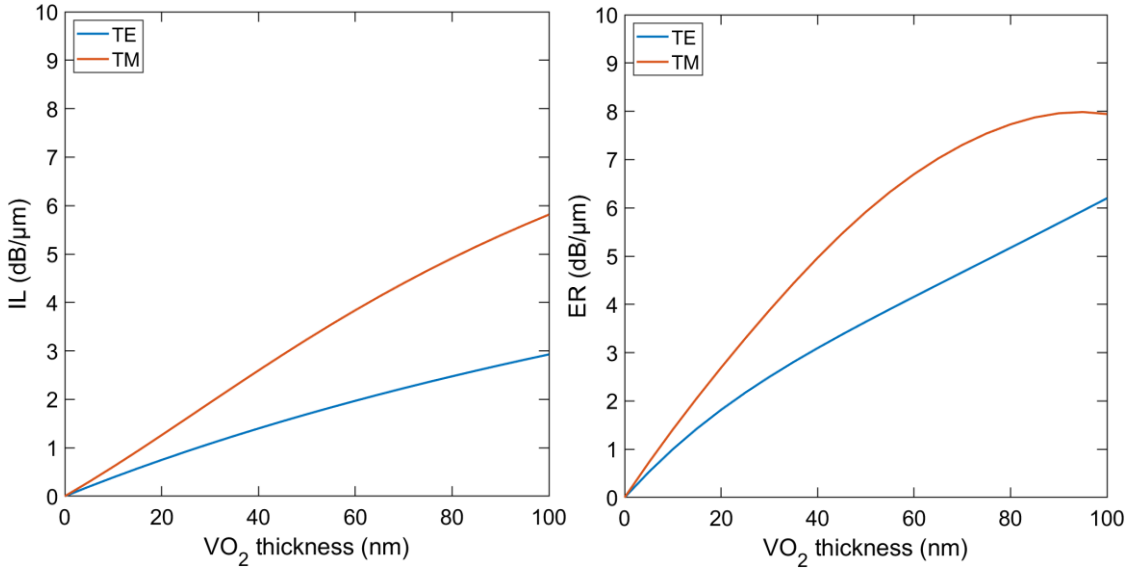


a) b)

**Figure 2.10.** a) Insertion losses (dB/μm) for polarizations TE and TM. b) Extinction ratio (dB/μm) for polarizations TE and TM.

In other ways, we can calculate the extinction ratio as the absolute difference between the propagation losses calculated for both states (2.3):

$$ER\left(\frac{dB}{\mu m}\right) = \left|\alpha_{i-VO_2} - \alpha_{m-VO_2}\right| \tag{2.3}$$

Using the above presented equation, we can now observe how the extinction ratio changes as a result of the increment of the $VO_2$ layer thickness (see Fig. 2.10.b). It can be observed that a higher extinction ratio is obtained for TM polarization. This is attributable to the fact that TM modes interact in a stronger way with the $VO_2$ layer due to their nature (see Fig. 2.6) since the layer is located on top the waveguide. Then, every variation that the $VO_2$ layer undergoes will affect more severely to TM propagated modes than it will do to TE modes.

### *2.3.2 Analysis of figure of merit (FOM) for TE and TM*

The next stage to effectively analyse what is the most suitable mode for the device being designed is to define a figure of merit (FOM). In this case, the FOM we will be using will consist of the quotient between the ER and the IL, and it will, therefore, be unitless (2.4).

$$FOM = \frac{ER\left(\frac{dB}{\mu m}\right)}{IL\left(\frac{dB}{\mu m}\right)} \tag{2.4}$$

Consequently, the FOM according to the fluctuation of the $VO_2$ layer thickness will result as it is shown (Figure 2.11):

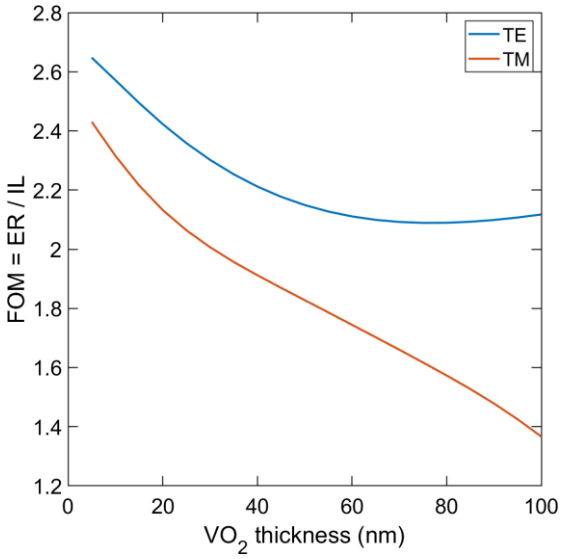


**Figure 2.11.** FOM for polarizations TE and TM.

By considering that both $VO_2$ on top and sides undergo the insulating to metal transition, a higher FOM is obtained for TE mode. This can be explained because that mode presents considerably lower insertion losses, which affect directly to the FOM calculation.

### *2.3.3 Discussion of final configuration and polarization*

However, when heating the hybrid waveguide by means of a microheater, changing only the $VO_2$ on top of the waveguide could be highly beneficial from the point of view of energy consumption and switching speed, due to the reduction of the heated region. So far, all the results shown were obtained by switching states of the upper $VO_2$ layer, as well as the layers on the sides. We will, in the next simulations, consider a scenario where only the top $VO_2$ layer changes its state to metallic. Following the previous process and calculations, these are the achieved ER and FOM (see Fig. 2.12). There is no need to re-calculate the IL since the hybrid waveguide will not undergo any changes in the i-$VO_2$ state:

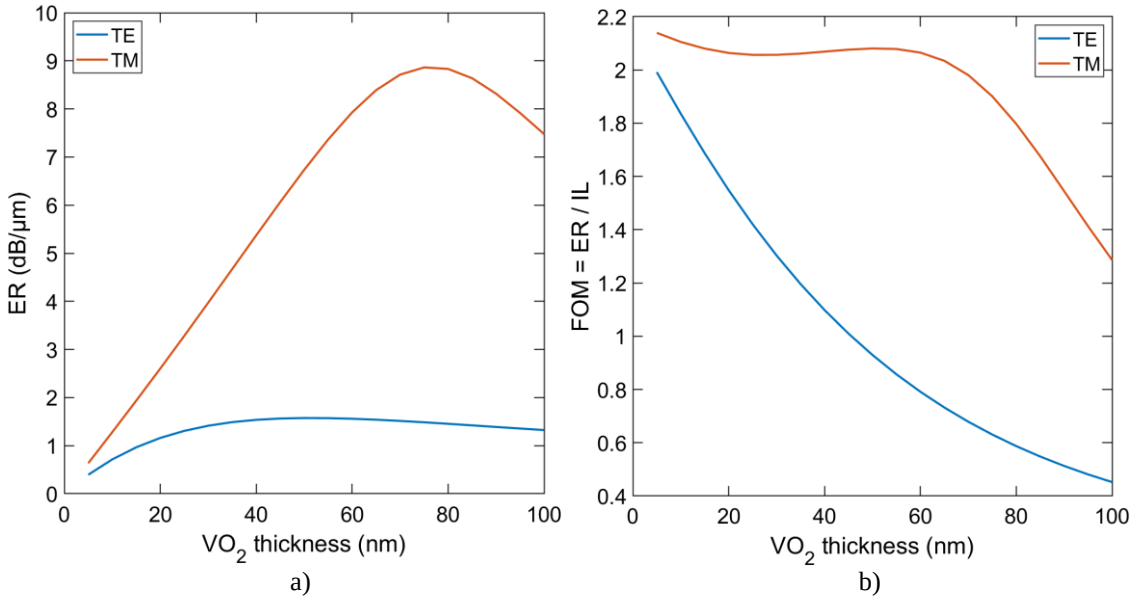


a) b)

**Figure 2.12.** Results when only the top $VO_2$ layer is heated: a) ER (dB/μm) and b) FOM.

In the last graphs, we can see that, when changing only the upper $VO_2$ layer state, a better ER and FOM are obtained for the TM polarization. In the other scenario (changing the state of all $VO_2$ layers), a better ER was attained for the TE polarization (see Fig. 2.10.b). In the next graphs, we can compare both scenarios for their best polarization (see Fig. 2.13):

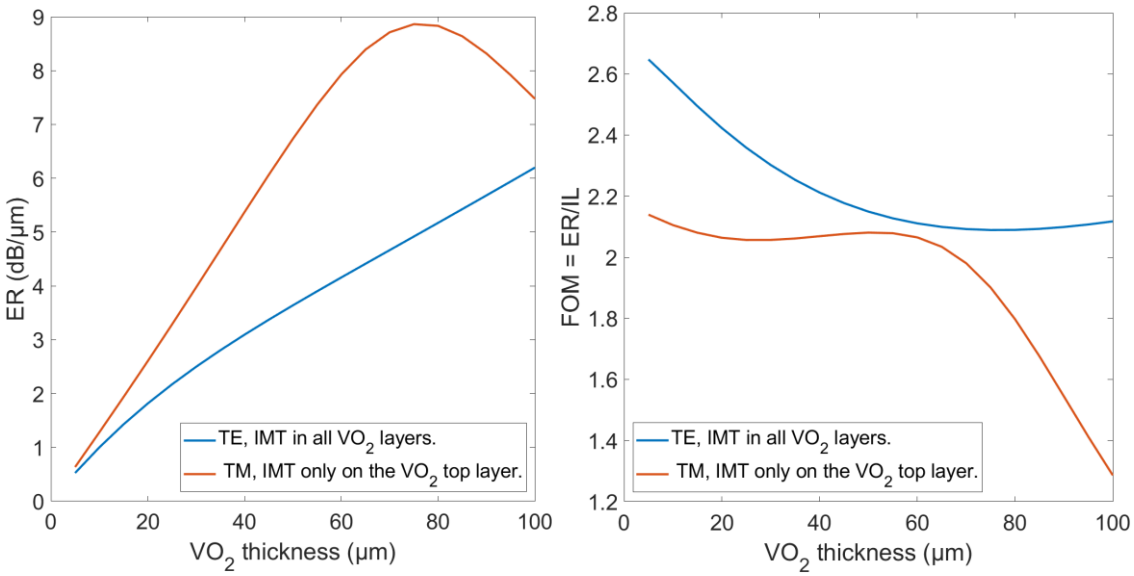


a) b)

**Figure 2.13.** Comparison for both scenarios: all $VO_2$ layer undergo IMT or only top $VO_2$ layer undergoes IMT. a) ER (dB/μm) and b) FOM.

While the FOM is slightly better for the TE polarization in the first case, ER (dB/μm) is considerably higher for TM polarization in the second scenario. A higher ER (dB/μm) means that shorter lengths will be needed to attain the same ER (dB), leading to more compact devices. This

is the reason that, from now on, we will be working assuming only state variation in the top $VO_2$ layer and working with the TM fundamental mode.

### *2.3.4 Analysis of optimal $VO_2$/Si waveguide length*

To attain the optimal length of the $VO_2$ layer, as well as its optimal thickness, we will set two possible values for the ER (dB) at which we want the device to perform properly. We will study the optimal length for both an ER = 10 dB and ER = 20 dB.

When setting the ER value to 10 dB, the optimal length can be calculated easily by dividing these 10 dB by the ER (dB/μm).

It is possible to similarly calculate the length for an extinction ratio of 20 dB. We are then able to represent the variation of the length according to the thickness of the $VO_2$ layer for both ER, leading to the following graphs (see Fig. 2.14):

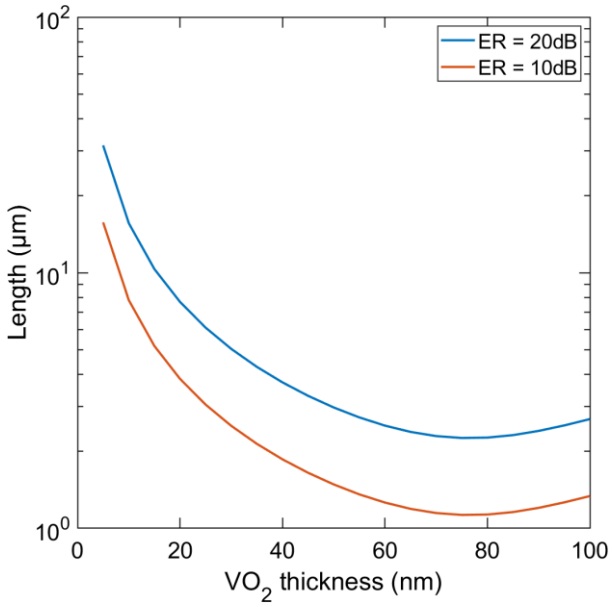


**Figure 2.14.** Optimal length (μm) in logarithmic scale according to $VO_2$ thickness for ER = 10 dB and ER = 20 dB for fundamental TM mode.

More specifically, the minimal lengths that can be obtained are, in the case of TM polarization, 1.13 μm and 2.26 μm for the ER = 10 dB and ER = 20 dB, respectively. In both cases, the $VO_2$ thickness is 75 nm.

In order to obtain the total insertion losses (dB) associated with the $VO_2$ lengths obtained, we will only need to multiply the previously calculated IL (dB/μm) (see Fig. 2.10.a) by these lengths (2.6).

As a result, the total insertion losses (dB) for both ER values and their correlated lengths are the following (see Fig. 2.15):

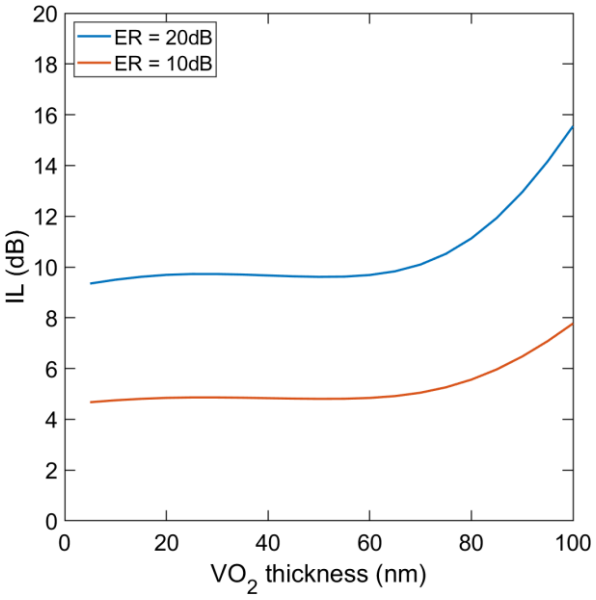


**Figure 2.15.** IL (dB) for TM mode for ER = 10 dB and ER = 20 dB.

Attending to the previous graph and focusing on the IL (dB) at 75 nm of $VO_2$ thickness, it can be observed that, for an extinction ratio of 10 dB, IL = 5.26 dB. On the other hand, for an ER = 20 dB, IL = 10.52 dB.

All the above presented information can be summarized in the following table (Table 2.2):

| ER (dB) | Length (μm) | Thickness (nm) | IL (dB) |
|---|---|---|---|
| **10** | 1.13 | 75 | 5.26 |
| **20** | 2.26 | 75 | 10.52 |

**Table 2.2.** Length (μm), thickness (nm) and IL (dB) for ER = 10 dB and ER = 20 dB.

## 2.4 Analysis of coupling losses for TM mode

### *2.4.1 Coupling losses for insulating and metallic states*

Once the insertion losses have been calculated, the next step is to verify that the insertion loss approximation is valid and thereby coupling losses are negligible, or, on the contrary, we need to redesign the device. For that matter, we will analyse the optical transmission of the hybrid waveguide using a 3D Finite Difference Time Domain (3D-FDTD) simulation. The simulator used will be the FullWAVE tool contained in RSoft.

The same way that was used for the effective indices calculation on FemSIM, it will be necessary to define a mesh with the divisions of the whole simulation region. In this case, the mesh used will also be non-uniform with the purpose of being accurate while computationally efficient. This mesh can be visualized in the following Figure 2.16:

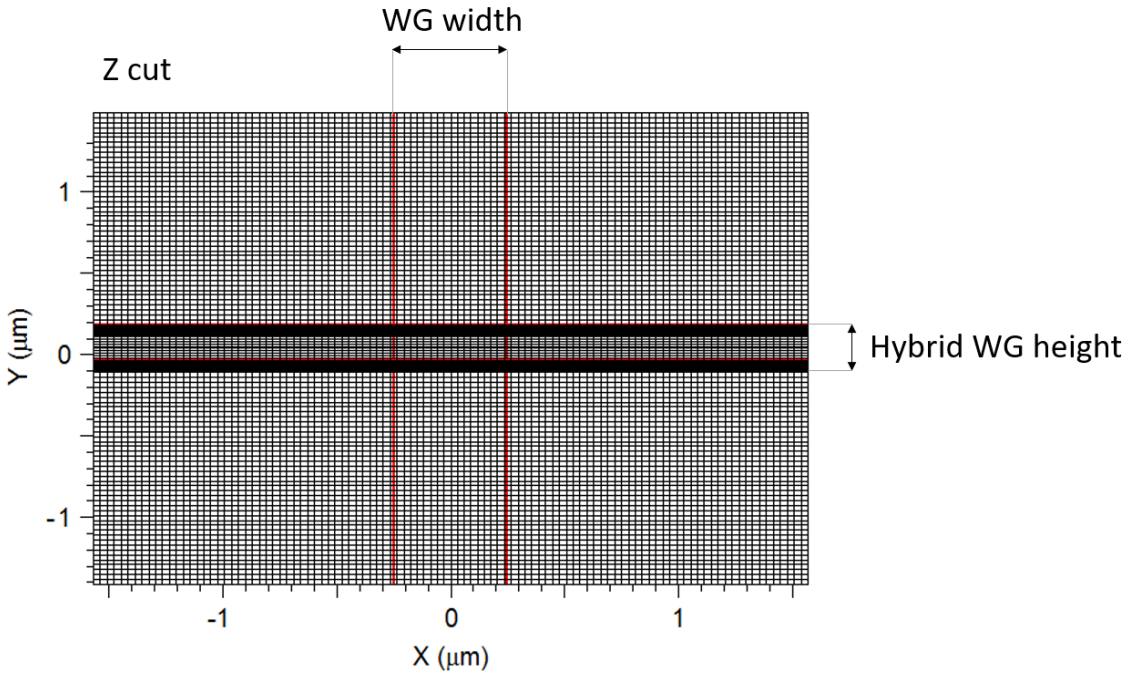


**Figure 2.16.** Non-uniform mesh for the FullWAVE 3D-FDTD simulation.

Furthermore, in order for FullWAVE to show the results of the losses, we need to introduce the monitors. Monitors are the defined surfaces that evaluate the characteristics of the light such as the optical power or field distribution. Three monitors will be defined.

The first one will be at the beginning of the waveguide, to check that the injected power is correct. A second one will be placed at the ending of the waveguide. This one measures the overlap power. The overlap measures the relative level of power in comparison to a reference one (launch field). In this case, we will measure the power that reaches the end of the waveguide against the total injected power. These two monitors will be used to calculate the insertion losses and the extinction ratio based on the obtained propagation losses.

The third monitor, on the other hand, will be located transversally throughout the length of the waveguide. The function of this monitor will be the to show the field distribution of the light wave travelling through the waveguide.

On Figure 2.17 it is shown a visual representation of the distribution of the monitors for the reader to comprehend how they have been placed.

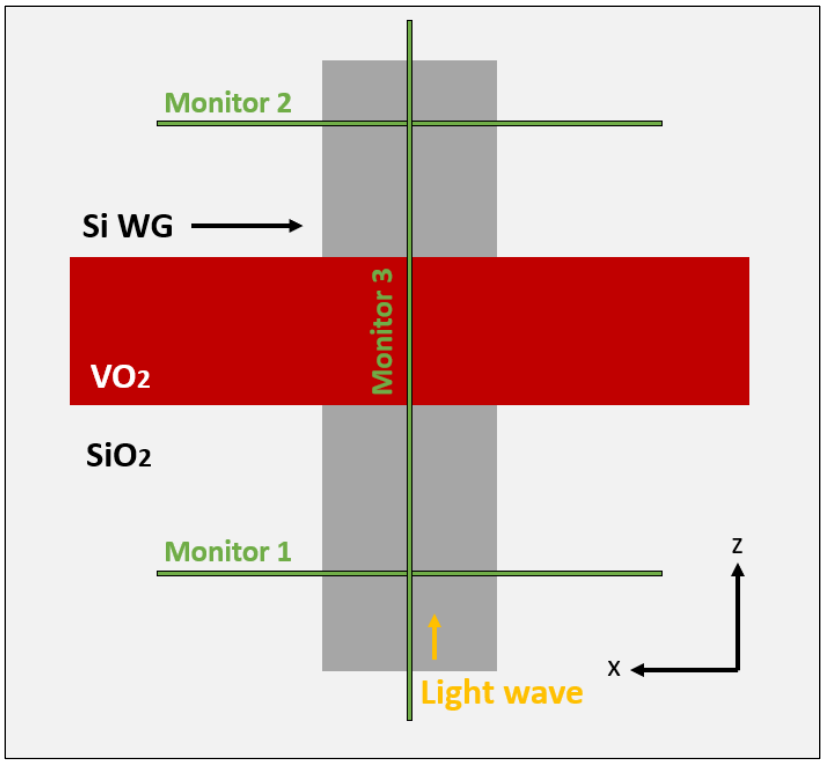


**Figure 2.17.** Monitors placement for the FullWAVE 3D-FDTD simulation. Top view.

With help from the second monitor, we will be able to see the level of power that reaches the end of the waveguide and calculate the total losses. We can compare this value with the previous IL calculated with FemSIM. The coupling losses will be the difference between these total losses and the IL obtained firstly.

After using FullWAVE to perform the 3D-FDTD simulation, the propagation of the light wave through the waveguide has been represented and it is below shown (see Figs. 2.18 and 2.19) for both the insulating and the metallic $VO_2$ states and for the ER = 10 dB model ($VO_2$ length = 1.13 μm).

As it was expected, when the $VO_2$ layer is in the insulating state, light propagates with low loss (see Fig. 2.18) compared to the high lossy metallic state (see Fig. 2.19).

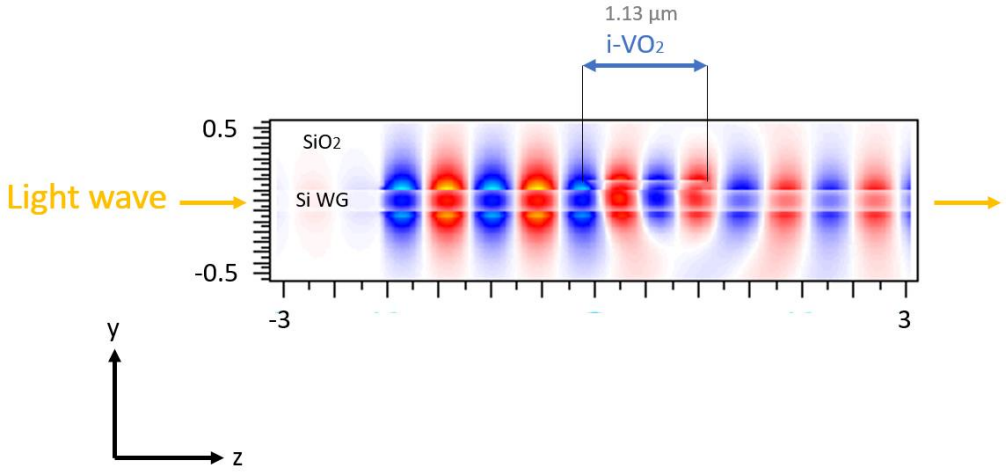


**Figure 2.18.** TM light wave propagation for i-$VO_2$ and $VO_2$ length = 1.13 µm.

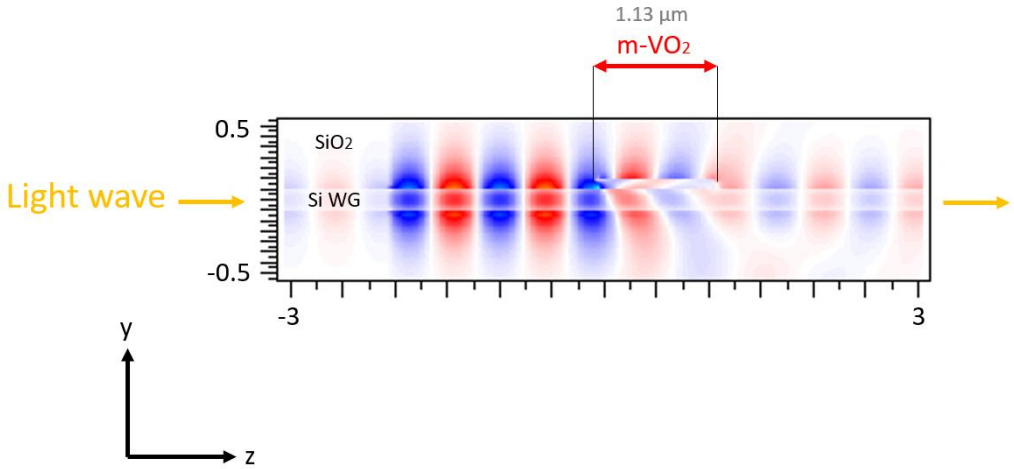


**Figure 2.19.** TM light wave propagation for m-$VO_2$ and $VO_2$ length = 1.13 µm.

After performing this simulation, we can analyse the insertion losses and extinction ratio that have been obtained by FullWAVE. In this case, IL = 6.27 dB and ER = 8.26 dB. Since we were expecting an ER of 10 dB, this is a moderately accurate result that fits into the desired performance of the designed model. The excess of losses can be attributed to the coupling losses that were not previously considered in the FemSIM simulations.

Moreover, when executing the same simulation for the case of ER = 20 dB ($VO_2$ length = 2.26 µm), the obtained 3D- FDTD results also differ from what was expected, being the actual results IL = 10.84 dB and ER = 18.31 dB. The higher losses are also caused by the existence of coupling losses.

The 3D-FDTD results when compared to the previous FemSIM results can be summarized in the following tables for both $VO_2$ lengths designs (Tables 2.3 and 2.4):

| | FEM (Effective index) | 3D-FDTD |
|---|---|---|
| **ER (dB)** | 10 | 8.26 |
| **IL (dB)** | 5.26 | 6.27 |

**Table 2.3.** Comparison of results for IL and ER for $VO_2$ length = 1.13 μm and $VO_2$ thickness = 75 nm.

| | FEM (Effective index) | 3D-FDTD |
|---|---|---|
| **ER (dB)** | 20 | 18.31 |
| **IL (dB)** | 10.52 | 10.84 |

**Table 2.4.** Comparison of results for IL and ER for $VO_2$ length = 2.26 μm and $VO_2$ thickness = 75 nm.

### *2.4.2 Redesign of the hybrid $VO_2$/Si waveguide*

Even so, when manufacturing the actual hybrid waveguide, minor imprecisions may occur; there is indeed a ± 10% possible deviation in the deposition of the $VO_2$ layer. It is needed to find the most robust design against these inaccuracies. If we look again at Figure 2.12.b, it can be observed that for a $VO_2$ thickness of 75 nm, any deviation can affect widely to the actual FOM. Then, it will be safer to use any value from the plane part of the graph. This way, the selected $VO_2$ thickness that will be used from now on is 40 nm.

Attending, once again, to the previous graphs where $VO_2$ length was displayed depending on its thickness (Fig. 2.14), it is obtained that, for an ER = 10 dB, the new length is equal to 1.86 μm. For an ER = 20 dB, on the other hand, the new length will be 3.72 μm. Therefore, there is a slight increment of less than 1 μm in the first case and roughly 1.5 μm in the second one. Nonetheless, we will now study how this change has affected to the insertion losses. It is easily calculated using FemSIM that the IL for this model are 4.83 dB and 9.66 dB, respectively. The redesign dimensions can be summarized in Table 2.5:

| ER (dB) | Length (μm) | Thickness (nm) | IL (dB) |
|---|---|---|---|
| **10** | 1.86 | 40 | 4.83 |
| **20** | 3.72 | 40 | 9.66 |

**Table 2.5.** Length (μm), thickness (nm) and IL (dB) for ER = 10 dB and ER = 20 dB when redesigning for $VO_2$ thickness = 40 nm.

After introducing the model with the new lengths in the 3D-FDTD simulation, the new obtained values are represented and compared with the FemSIM results in Tables 2.6 and 2.7:

| | FEM (Effective index) | 3D-FDTD |
|---|---|---|
| **ER (dB)** | 10 | 8.9 |
| **IL (dB)** | 4.83 | 5.09 |

**Table 2.6.** Comparison of results for IL and ER for $VO_2$ length = 1.86 μm and $VO_2$ thickness = 40 nm.

| | FEM (Effective index) | 3D-FDTD |
|---|---|---|
| **ER (dB)** | 20 | 22.14 |
| **IL (dB)** | 9.66 | 10.08 |

**Table 2.7.** Comparison of results for IL and ER for $VO_2$ length = 3.72 μm and $VO_2$ thickness = 40 nm.

It can be observed in the latter tables that extinction ratio is similar to what was expected. Besides, the insertion losses also resemble more accurately what FemSIM previously calculated, that meaning the new coupling losses are also lower.

Lastly, and even though the design has been originally planned to work for C-band central wavelength (λ = 1.55 μm), a study has been conducted to analyse the performance of the hybrid waveguide the whole range of C-band wavelengths. This study has also been performed using FullWAVE and it shows wavelengths ranging from 1.5 μm to 1.6 μm (see Fig. 2.20).

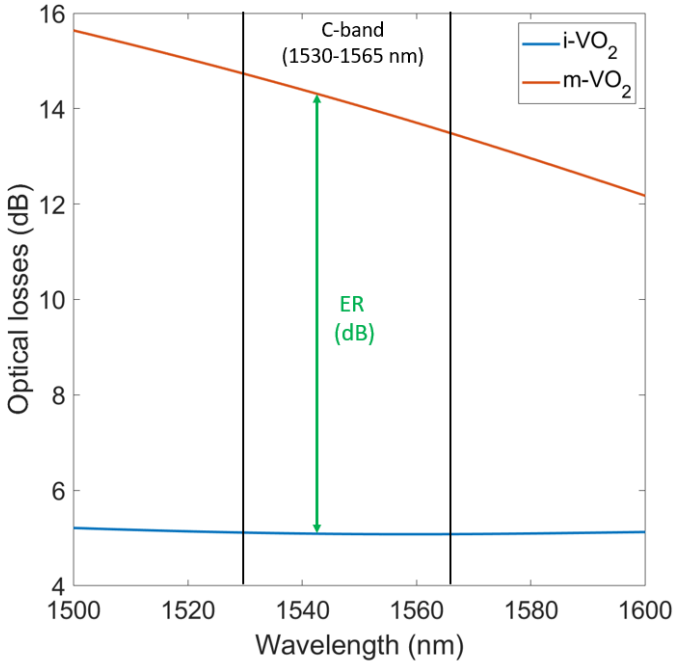


a)

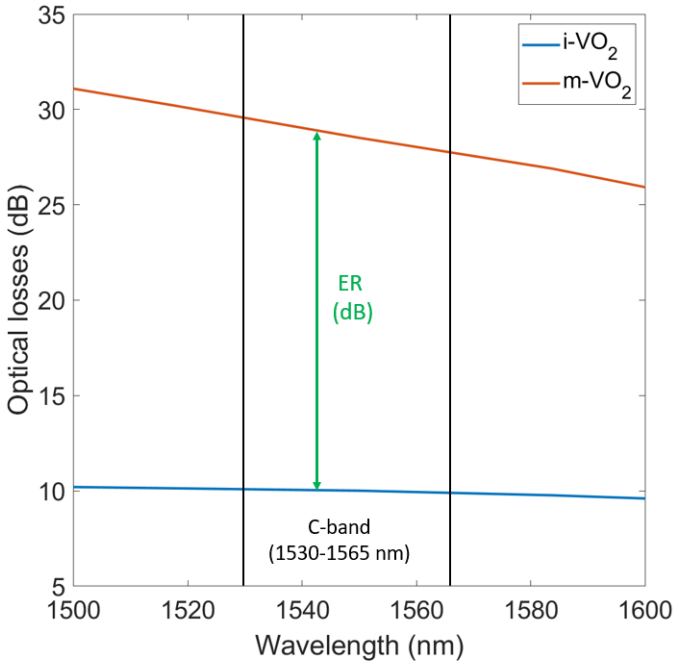


b)

**Figure 2.20.** Optical losses in the C-band for $VO_2$ hybrid waveguide length of: a) 1.86 μm (expected ER = 10 dB) and b) 3.72 μm (expected ER = 20 dB).

In the previous graphs, it can be seen that, while the IL (i-$VO_2$ optical losses) remain constant, the ER decreases slightly with the increase of the wavelength. This can be attributed to the fact that the confinement of the mode changes with the frequency, and so the interaction between light and the $VO_2$ layer also changes, generating slightly less optical losses in the m-$VO_2$ case.

As a final conclusion for Chapter 2, it can be affirmed that an efficient and robust configuration for the hybrid waveguide has been achieved. While the $VO_2$ layer thickness will be 40 nm, its length will be 1.86 μm when expecting a 10-dB-ER, or 3.72 μm for a 20-dB-ER. We have also discerned that it will be only necessary to switch the state of the $VO_2$ patch placed on top of the Si waveguide, while the $VO_2$ side patches can remain in i-$VO_2$ state. In fact, as it has been shown, optical performance will be even better with this state configuration (see Fig. 2.13).

The next step in the optimal switching device design will be to obtain the best heater configuration in order to minimize its impact on the optical features, while saving as much energy as possible. Such study will be analysed in the following Chapter 3.

# Chapter 3. Design of the heating system

## 3.1 Design of hybrid waveguide with metallic heaters

As it was stated in Chapters 1 and 2, for the $VO_2$ to change states and therefore, the optical switching to occur, one way to achieve this is, among others, to heat the material. More specifically, the IMT temperature oscillates around 65ºC. To achieve such local heating, a microheater is usually employed. The microheater consists of a metallic resistor that heats up using Joule heating (see Fig. 3.1). For this work, we will consider titanium (Ti) as the metal used for the heater. In the following chapter it will be discussed the main physical characteristics of the heater, as well as its optimal configuration in order to minimize optical losses.

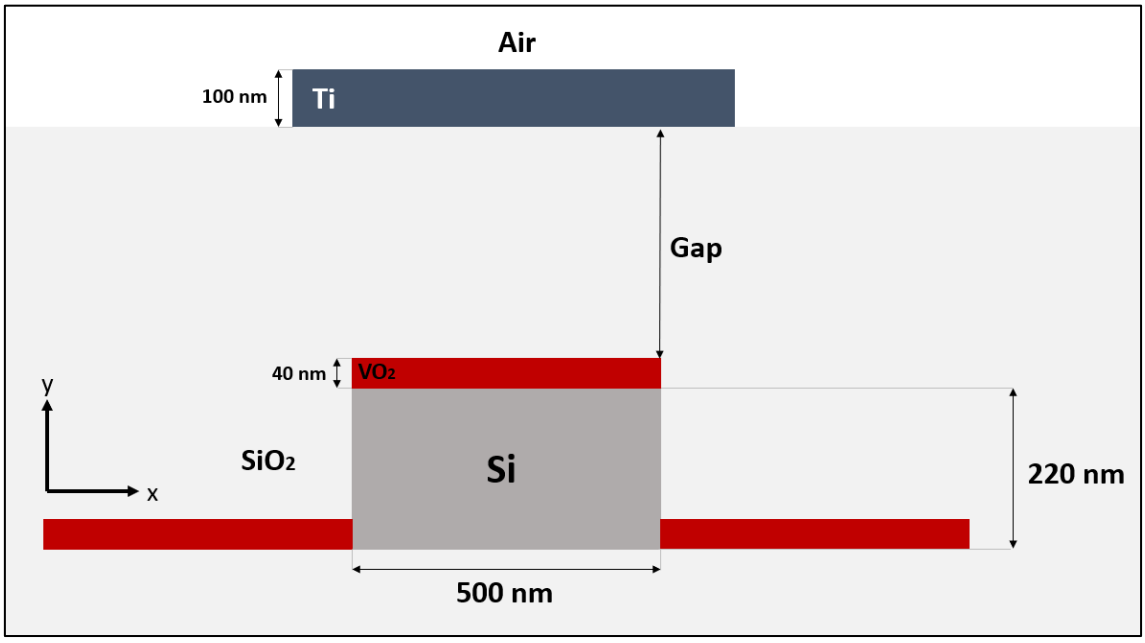


**Figure 3.1.** Cross-section and dimensions of the hybrid waveguide and heater configuration.

### *3.1.1 Discussion of optimal heater placement*

While there are several configurations to place the Ti heater with respect to the hybrid waveguide, in this project we chose to place it on top of the hybrid $VO_2$/Si waveguide (see Fig. 3.2). This is mainly due to the heat transfer physics. Since the heat is propagated from the centre of the Ti heater, the waveguide should be as close as possible to this point, so as to minimize the power consumption. Besides, the heater centre must be aligned with the waveguide centre for the same reason.

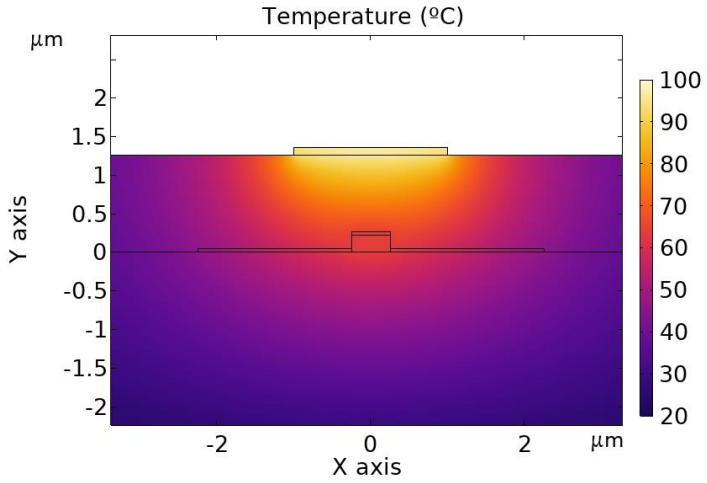


**Figure 3.2.** Heat transfer when placing the heater on top of the waveguide. The distance between the heater and the $VO_2$/Si waveguide is 1 µm.

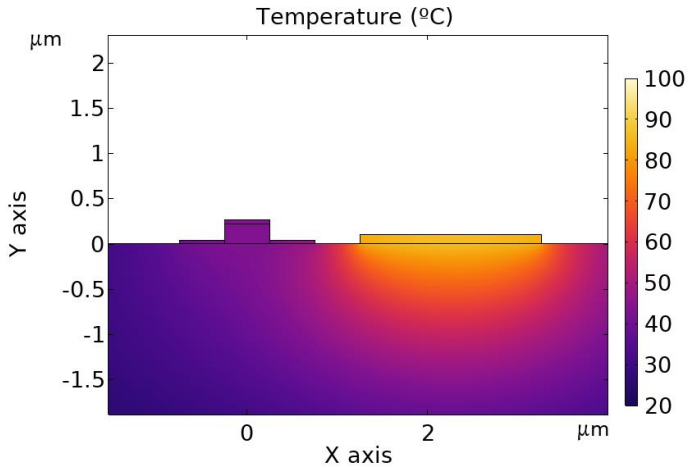


**Figure 3.3.** Heat transfer when placing the heater in one of the sides of the waveguide.

It could also be possible to put the microheater on one of the sides of the waveguide. Placing the heater in one of the sides would result in a non-uniform heating of the $VO_2$ layer; the closest side to the heater would heat earlier (see Fig. 3.3).

### *3.1.2 Optimization of gap for low losses*

Since the heater is made up of titanium, and this material is not optically transparent, placing it too close to the hybrid waveguide may introduce additional losses making the device less efficient. It is then necessary to introduce a certain distance between the heater and the waveguide. This heater-waveguide distance is the gap.

On the other hand, the thickness of the Ti heater will be established at 100 nm and its length will be the same as the $VO_2$ patch length. The cross-section for this design can be observed in Figure 3.1.

For this analysis, we will consider the previous redesign, i.e, a 40-nm thick $VO_2$ layer switching only the fragment that is placed on top of the Si waveguide. Hence, we will study the effects on the propagation losses for both states i-$VO_2$ and m-$VO_2$. The purpose of this study is to find the minimal gap distance that allows the heater to be optically transparent to the optical mode. That is, the minimal distance at which the propagation losses remain unaltered. For that matter, we will carry out a simulation sweep using FemSIM, varying the gap from 0 to 2 μm, with a step of 0.1 μm.

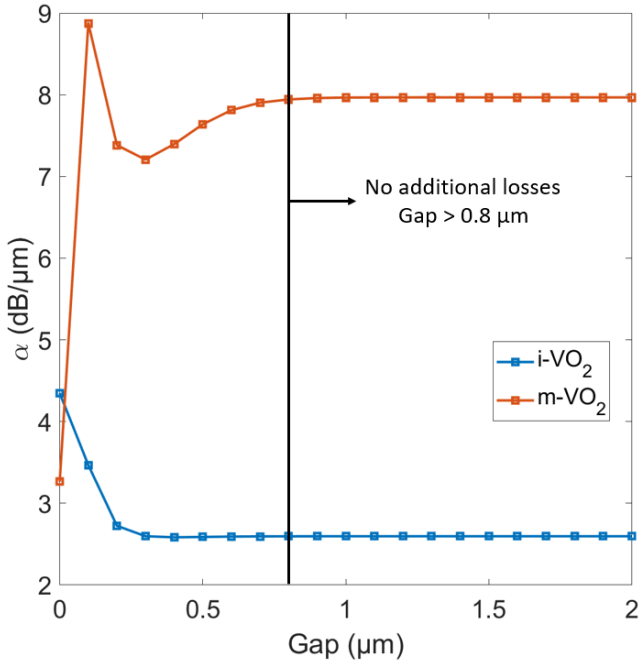


**Figure 3.4.** TM fundamental mode propagation losses, α, for $VO_2$ thickness = 40 nm.

We can see in Figure 3.4 that the gap between the heater and the hybrid waveguide does only affect when the heater is placed too close to the hybrid waveguide. Specifically, for any distance larger than 0.8 μm, propagation losses do not depend on the gap for any of the states.

It is logical to believe that the losses at the constant part of the graph coincide with those when no heater was used. This can be verified by looking again at Figure 2.9, for a $VO_2$ thickness of 40 nm. The exact value for the propagation losses with i-$VO_2$ and m-$VO_2$ are 2.60 dB and 7.97 dB, respectively.

In the following images (see Fig. 3.5) we depicted, using FemSIM, how the TM mode is affected by the influence of the Ti heater. These simulations have been carried out for gaps = 0.2 μm, 0.8 μm and 1.5 μm.

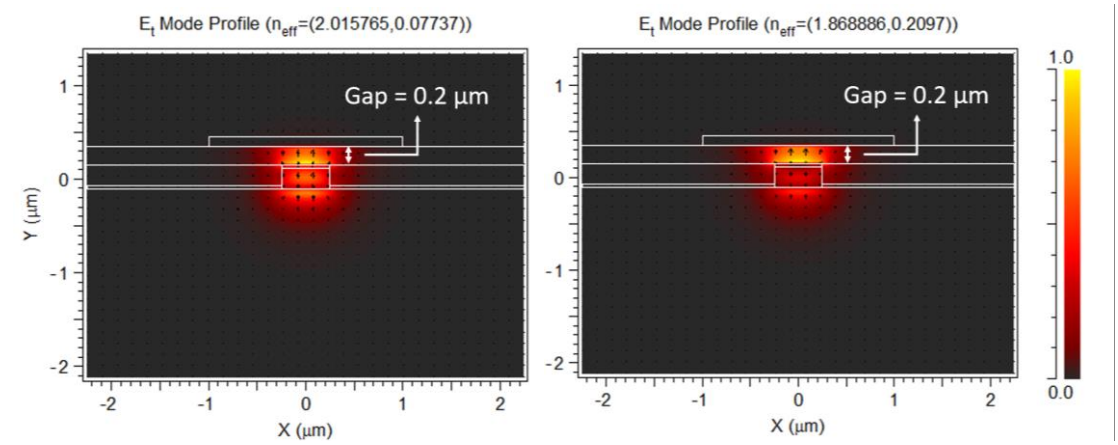


a.1) a.2)

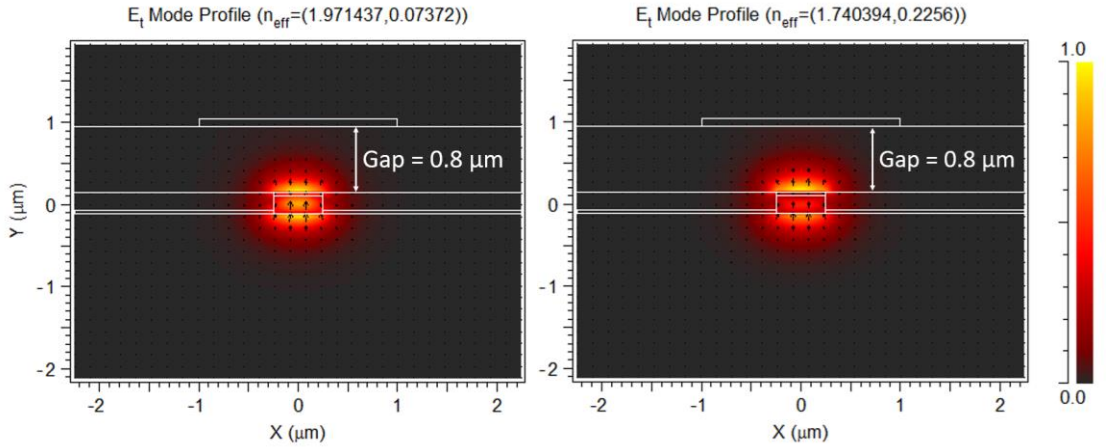


b.1) b.2)

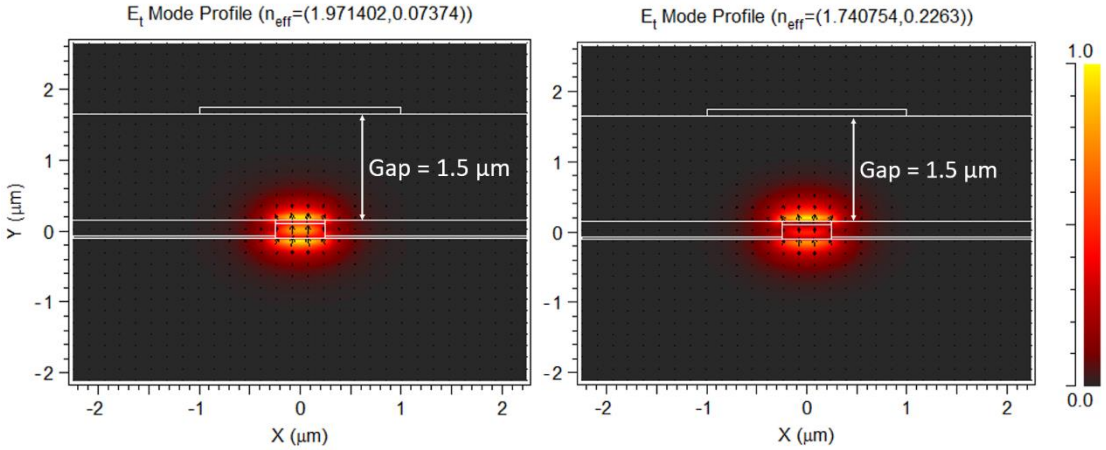


c.1) c.2)

**Figure 3.5.** TM mode propagations with i-$VO_2$ (left) and m-$VO_2$ (right) layer for gaps: a) 0.2 µm, b) 0.8 µm and c) 1.5 µm.

In the above shown images, it can be seen that for gaps larger than 0.8 µm, the Ti heater does not affect to the TM mode. However, for lower gaps (Fig. 3.5.a), TM mode suffers a slight variation and its effective refractive index is increased.

## 3.2 Analysis of performance metrics

Once the optical influence of the heater has been studied, the next step its design will require is to obtain the minimum power needed to achieve the state transition, as well the minimum time to reach the switching temperature.

### *3.2.1 Simulation of thermal profile*

In order to carry out this study, it is important to remember that the required temperature to reach the $VO_2$ state transition is around 65ºC. Therefore, a heater will be used to rise the patch temperature. Said heater consists of a Ti layer which will be applied an electrical current so as to produce heat according to the Joule effect. This heat is meant to reach the hybrid waveguide and increase the $VO_2$ temperature. The equation of the heat propagation is the following (3.1):

$$\nabla(-k_T \nabla T) + \rho_T c_T \frac{\partial T}{\partial t} = q_s \tag{3.1}$$

where $k_T$ stands for the thermal conductivity ($\frac{W}{m \cdot K}$), $\rho_T$ stands for the density of the material ($\frac{kg}{m^3}$), and $c_T$ is the heat capacity ($\frac{J}{kg \cdot K}$). On the other hand, T is the temperature (K), and $q_s$ is the power density generated by the heat source ($\frac{W}{m^3}$).

Also, the power density ($q_s$) produced by the Ti heater can be described by the following equation (3.2):

$$q_s = \frac{P_i}{l_h * w_h * t_h} \left(\frac{W}{m^3}\right) \tag{3.2}$$

where $l_h$, $w_h$ and $t_h$ are the dimensions of the titanium heater (length, width, and thickness, respectively). $P_i$ stands for the electric power consumed by the heater.

The thermal properties of the materials used in the simulations are described in the following Table 3.1:

| Material | $k_T$ (W m$^{-1}$ K$^{-1}$) | $\rho_T$ (kg m$^{-3}$) | $c_T$ (J kg$^{-1}$ K$^{-1}$) |
|---|---|---|---|
| **Si** | 163 [18] | 2330 [18] | 703 [18] |
| **$SiO_2$** | 1 [18] | 2203 [18] | 650 [18] |
| **Ti** | 23 [19] | 4500 [20] | 523 [21] |
| **$VO_2$** | 3.5 [22] | 4571 [22] | 356 [22] |

**Table 3.1.** Thermal properties for λ = 1550 nm and T = 293.15 K.

The heat simulations will be carried out using the COMSOL Multiphysics software. Among the several features contained in this software, we will use the heat propagation tool.

The next step is to define the boundary conditions, such as the room temperature and the heat transfer coefficient, both in the upper boundary of the simulation region. The first one will be set at 20ºC (293.15K), while the latter will be h = 15 $(\frac{W}{m^2} * K)$. The heat will be transferred by convection in the air surface.

Lastly, as well as in the previously performed FemSIM simulations, a mesh must be defined. As in such cases, we will use a non-uniform mesh to achieve a higher precision in the heater and $VO_2$/Si waveguide. In this case, COMSOL by default divides the simulation region in tetrahedrons whose size varies. The mesh used for these simulations is shown in the next images (see Fig. 3.6). We can observe that the grid is more precise in the $VO_2$ layer and its adjacent regions, while it is coarser in the $SiO_2$ substrate.

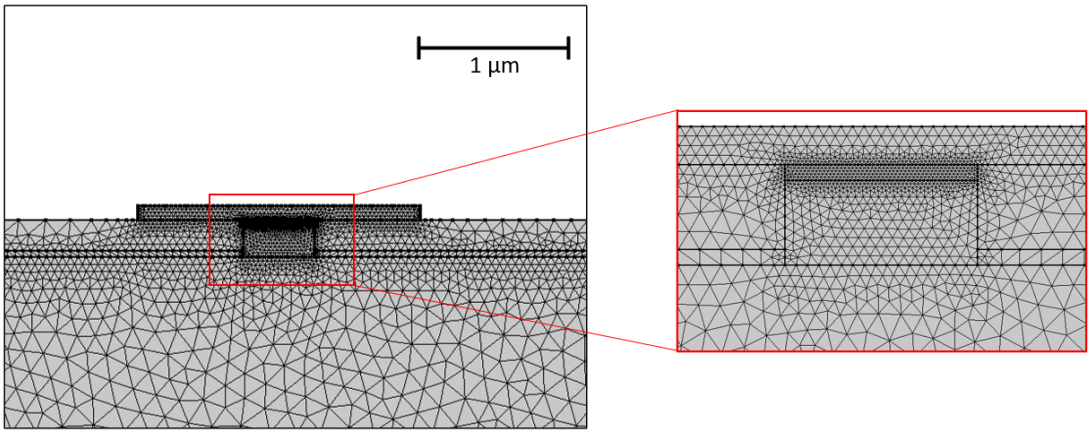


**Figure 3.6.** Non-uniform mesh used in the COMSOL simulations.

We can visually observe how the heat is propagated from the heater through the cladding until it reaches the hybrid waveguide, and, intuitively, confirm that higher temperatures are attained closer to the heater. As mentioned in section 3.1.1, since the highest temperatures are reached in the centre of the heater, the heater must be aligned with the waveguide, so as to maximize the heat transfer. The simulation has been initially carried out for gaps = 0, 0.8 and 2 µm. The injected power in the heater is 1 mW (see Fig. 3.7).

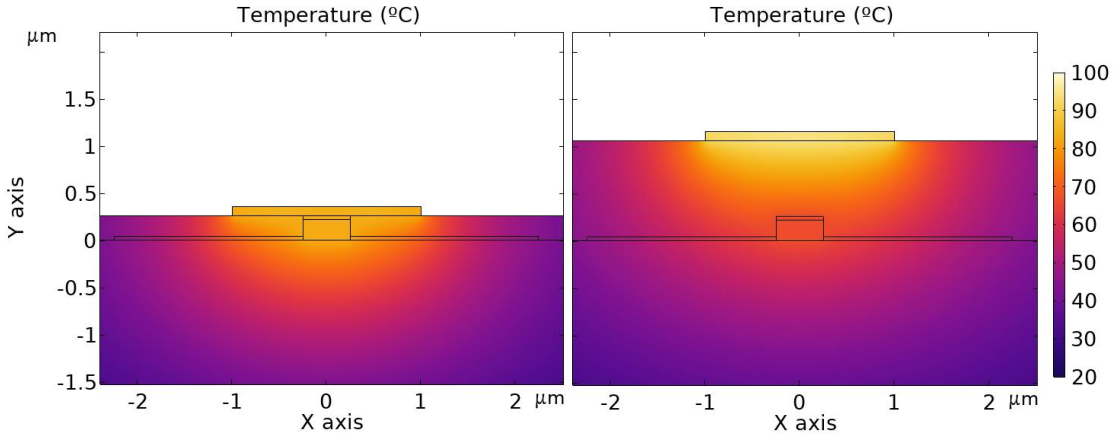


a) b)

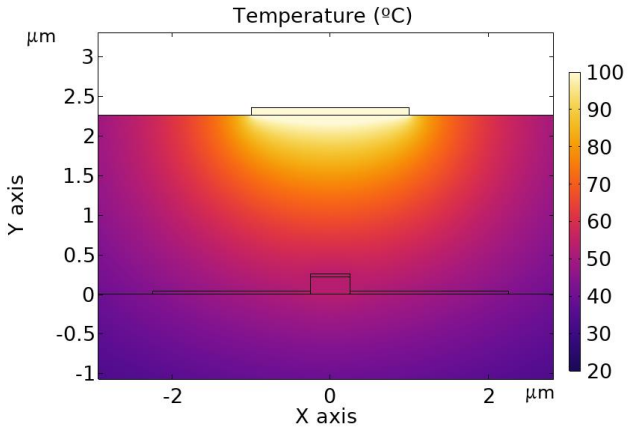


c)

**Figure 3.7.** Thermal profile of the Ti heater- hybrid waveguide configuration when $P_i$ = 1 mW for gaps: a) 0 µm, b) 0.8 µm and c) 2 µm.

We can more precisely observe how the temperature in the $VO_2$ layer decreases as the gap increases in the graph shown in Figure 3.8.

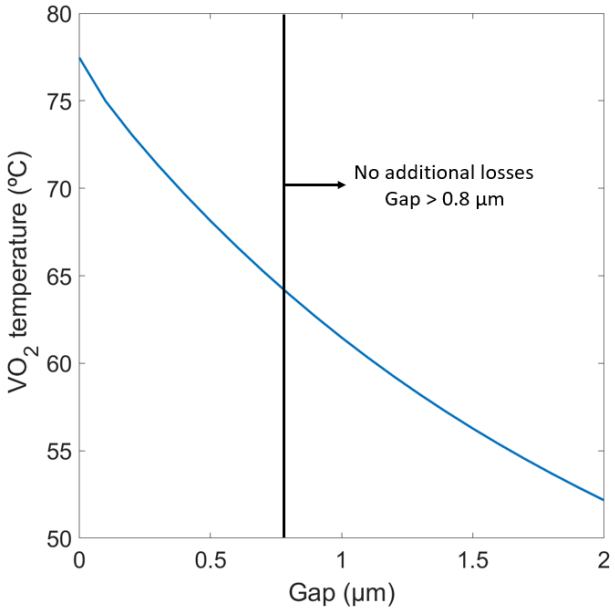


**Figure 3.8.** $VO_2$ temperature (ºC) depending on the $VO_2$ layer – Ti heater gap (µm) when $P_i$ = 1 mW.

### *3.2.2 Calculation of power consumption and switching time*

The previously shown graph contained the results of a simulation for an injected power of 1 mW in the heater. Since the temperature depends linearly on the injected power, it can also be calculated the coefficient at which the temperature varies with every mW injected (3.4). From now on, this will be considered as the thermo-electrical coefficient ($a$).

$$T\ (^{o}\mathrm{C}) = a\ \left(\frac{^{o}\mathrm{C}}{\mathrm{mW}}\right) * Pi(mW) + b\ (^{o}\mathrm{C}) \tag{3.4}$$

Assuming that $b$ = 20ºC, $a$ (ºC/mW) is obtained for all the range of temperatures that have been calculated according to every gap. Thus, the thermo-electrical coefficient can be represented depending on the gap, as it is shown in Figure 3.9. The conversion of electrical power into heat in the $VO_2$ will be less efficient if we increase the distance between the layer and the Ti heater due to the temperature gradient:

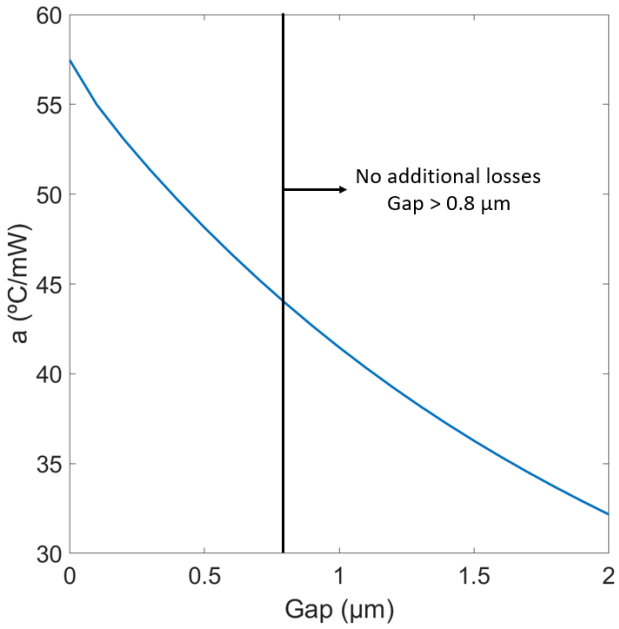


**Figure 3.9.** Thermo-electrical coefficient (ºC/mW) depending on the $VO_2$ layer – Ti heater gap (µm).

Now that the thermo-electrical coefficient has been calculated for every possible gap considered, it can be similarly found, using again equation 3.1, the required power so as to achieve a $VO_2$ temperature of 65ºC for all of these gap values (see Fig. 3.10). As it is also obvious from the previous results, more injected power will be necessary to achieve 65ºC in the $VO_2$ layer if the gap is increased:

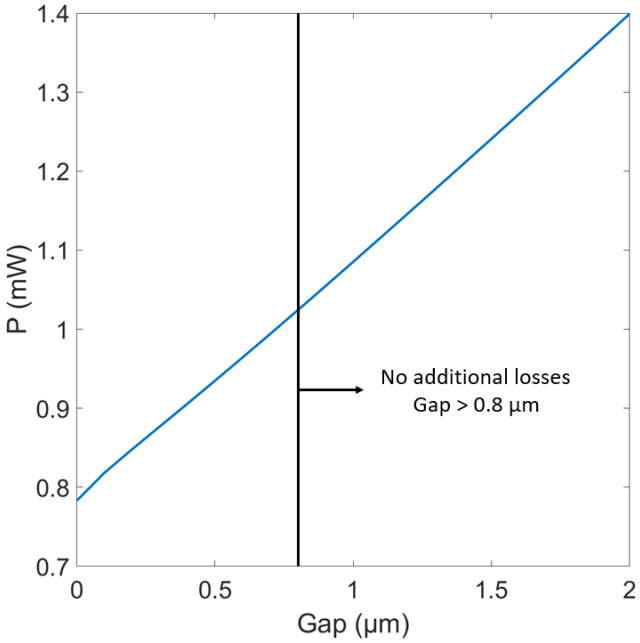


**Figure 3.10.** Necessary electrical power to achieve 65ºC on the $VO_2$ layer, depending on the $VO_2$ layer – Ti heater gap (μm).

Knowing this, the most logical solution is to locate the Ti heater as close as possible to the hybrid waveguide. Nonetheless, it was discussed in section 3.1.2 that if the heater is too close (about <0.8 μm), the optical features of the titanium can affect the light propagation and increment the losses. For this reason, it is needed to meet a trade-off between these two conditions. This is, the gap between the heater and the waveguide must be set large enough so as not to introduce additional losses, and, on the other hand, small enough to minimize the power consumption.

However, it does not only matter how much power is needed in a given time instant, but also the time that this power needs to be supplied. This is the consumed energy; the power consumption by the time during which it was consumed (3.5):

$$E(J) = Pi\,(W) * t(s) \tag{3.5}$$

Therefore, the next section will address the study of the time needed to achieve the transition temperature (rise time), and then, the state switching. For that matter, we will perform a sweep for all the gap range considered previously and observe what is their associated temperature achieved in the $VO_2$ layer.

Besides, it is also remarkable that the used pulse duration (this is, the time during which the power has been injected) is 100 μs (see Fig. 3.11):

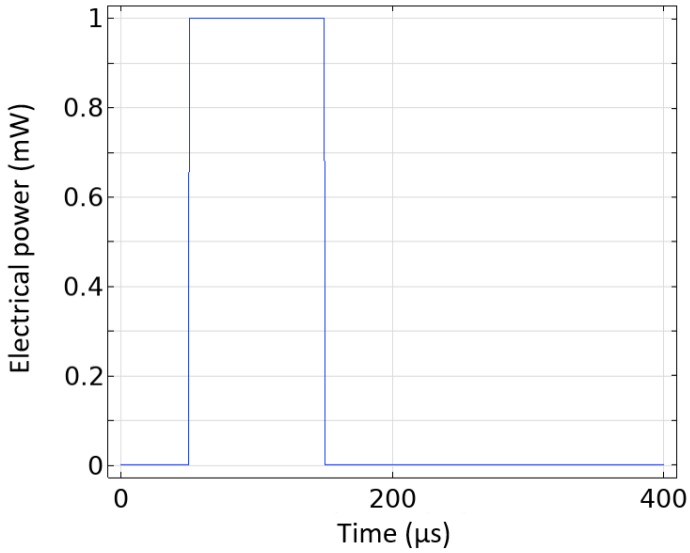


**Figure 3.11.** Injected power pulse in the COMSOL simulator.

This can also be observed in Figure 3.12, since temperature starts rising at time = 50 µs, and it does not start falling until time = 150 µs. This also states an important fact about $VO_2$ state-switching conditions; for the material to remain in m-$VO_2$ state, it must be kept heated for as long as it is wanted in such state. Figure 3.12 shows how the $VO_2$ temperature varies through the time for every gap.

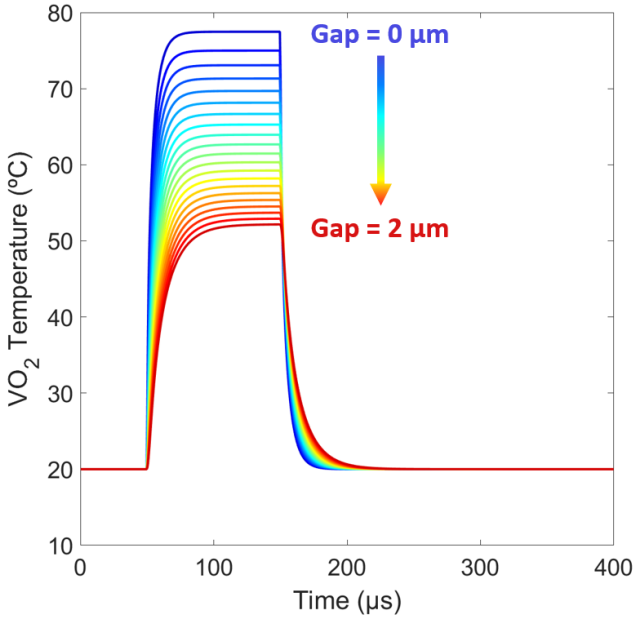


**Figure 3.12.** Time variation of $VO_2$ temperature for gaps varying from 0 µm (pink) to 2 µm (yellow) with a step of 0.1 µm.

In the above shown graph it can be observed that for larger gaps, the temperature takes slightly larger times to stabilize around its maximum value. Besides, another relevant point to be seen is that rise and fall times are very similar. This means that smaller gaps make the $VO_2$ layer heat

and cool in less time than larger ones. This can be observed with more detail in the following graphs (see Fig. 3.13):

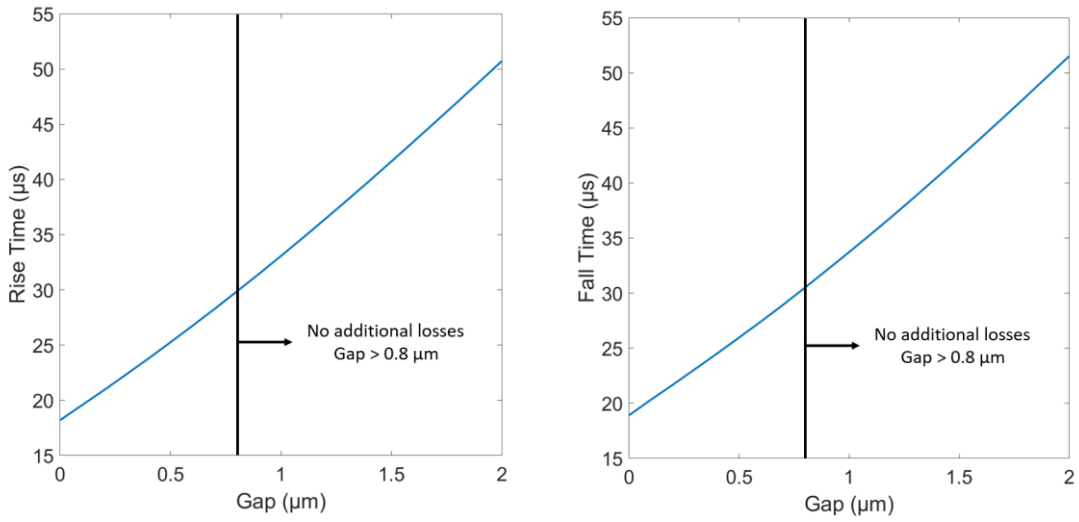


a) b)

**Figure 3.13.** Time (µs) needed to: a) achieve maximum temperature (Rise Time) and b) return to room temperature (Fall Time), depending on the gap (µm).

In the last instance, it is possible to obtain the temporal graphs for every gap when the injected power is the necessary power to attain 65ºC in the $VO_2$ layer (shown in Figure 3.10). When these simulations are carried out, the resulting graph should show that with independence of the gap used, all $VO_2$ temperatures must converge at 65ºC. This can be checked in Figure 3.14:

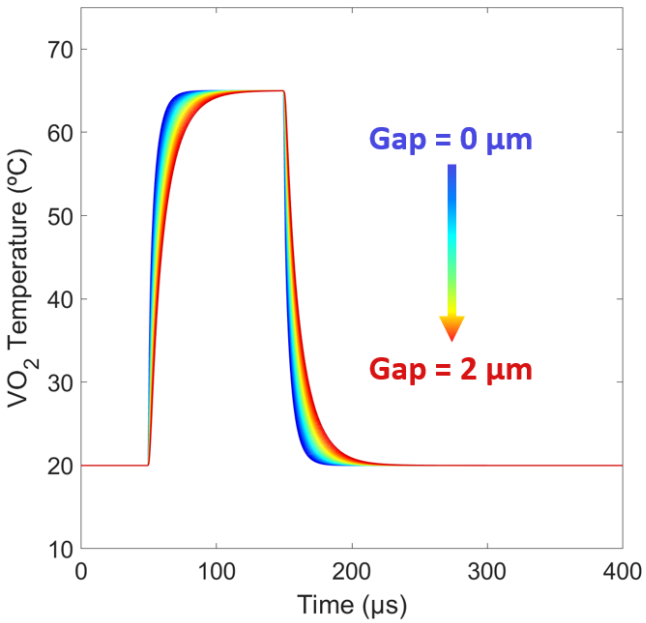


**Figure 3.14.** Time variation of $VO_2$ temperature when the injected power is the one needed for $VO_2$-Temperature = 65ºC, for gaps varying from 0 µm (pink) to 2 µm (yellow) with a step of 0.1 µm.

As expected, the results are quite similar to the ones shown in Figure 3.12, since the heating process remains the same, but with the sole difference that in this case, the injected power is the one needed to achieve 65ºC in the $VO_2$ layer. Hence, none of the simulations reach any higher (or lower) than this. As before, it can be appreciated that for larger gaps, it takes longer rise and fall times, which, in the end, lead to higher energy consumptions, since the power needs to be injected for a longer period of time.

## 3.3 Summary of final design

As a conclusion for Chapter 3, the main features of the heater – $VO_2$/Si waveguide configuration will be listed. We already established in Chapter 2 the dimensions for the hybrid waveguide (see Table 2.5). A standard 220x500-nm Si waveguide will be used. The $VO_2$ patch placed on top of it will be 40-nm thick. Its length will be either 1.86 μm for an ER = 10 dB, or 3.72 μm for an ER = 20 dB and it is optimised for the fundamental TM mode.

On the other hand, it is important to enumerate the Ti heater distances and dimensions. We have concluded that the minimum gap distance between the heater and the waveguide that does not introduce any additional propagation losses is 0.8 μm. Besides, the heater length will coincide with the one of the $VO_2$ patch. The heater thickness has also been set at 100 nm. The needed injected power in the heater to obtain 65ºC in the $VO_2$ layer can be seen in Fig. 3.10 and it is 0.994 mW. The MIT/IMT will happen within 29.85 μs (see Fig. 3.13). With all this information, the final design can be visualized in the following Figs. 3.15 and 3.16:

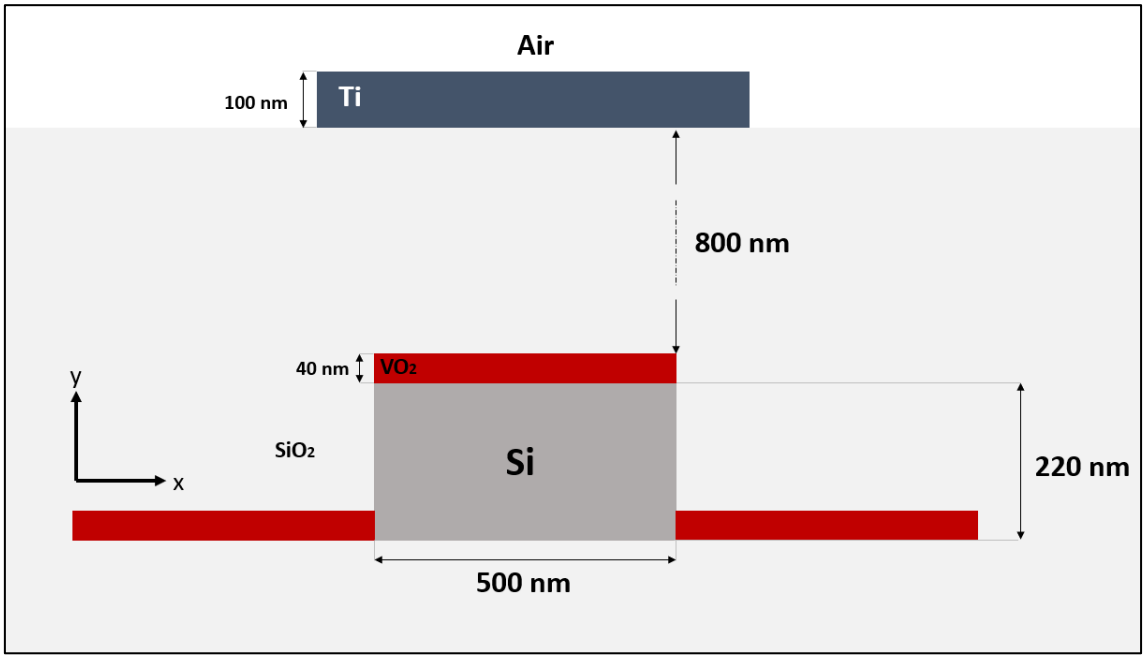


**Figure 3.15.** Cross-section of the final configuration of the Ti heater – hybrid $VO_2$/Si waveguide.

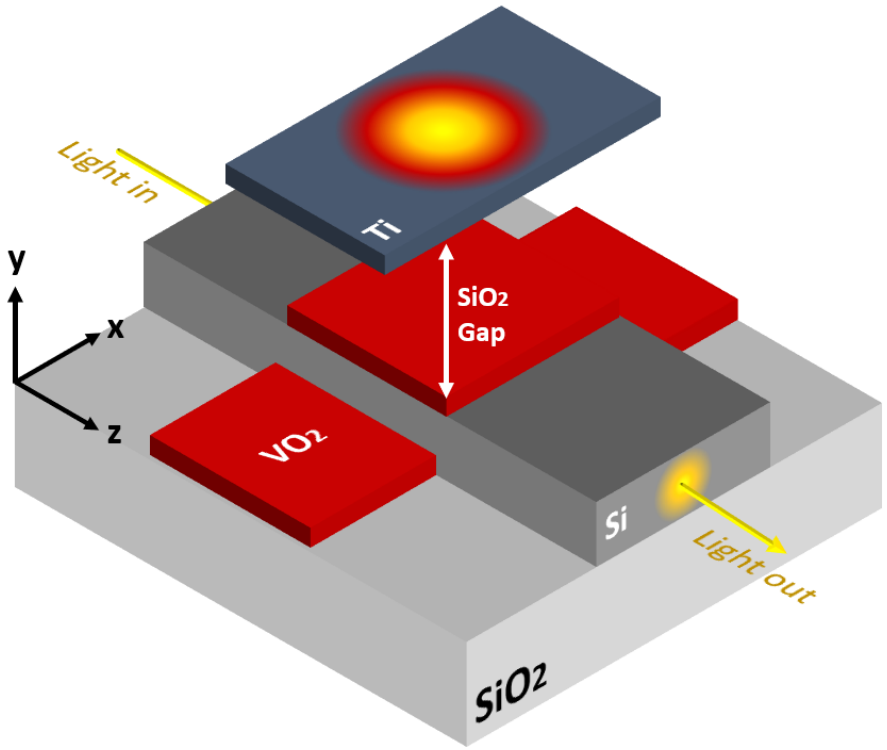


**Figure 3.16.** 3D representation of the final configuration of the Ti heater – hybrid $VO_2$/Si waveguide.

# Chapter 4. Fabrication and experimental results

The aim of this chapter is to experimentally analyse the response to the thermal stimulus of the designed hybrid $VO_2$/Si waveguide. However, a preliminary design will be characterized, without the Ti heater and the $SiO_2$ cladding. It will consist of a 2-µm-long $VO_2$/Si hybrid waveguide. As described in previous chapters, a change in the temperature of the $VO_2$ layer will result in a variation of its state (IMT – MIT). This will vary its refractive index, therefore resulting in a higher absorption of light, and making the device act as a switch. We will analyse the hybrid waveguide response in the C-band spectrum when the $VO_2$ temperature varies through the desired range (20ºC – 80ºC).

## 4.1 Description of the fabrication process

The first step in order to perform these measurements is to obtain the physical testing device. The fabrication process of the $VO_2$/Si hybrid waveguide is depicted in the following diagram shown in Fig. 4.1:

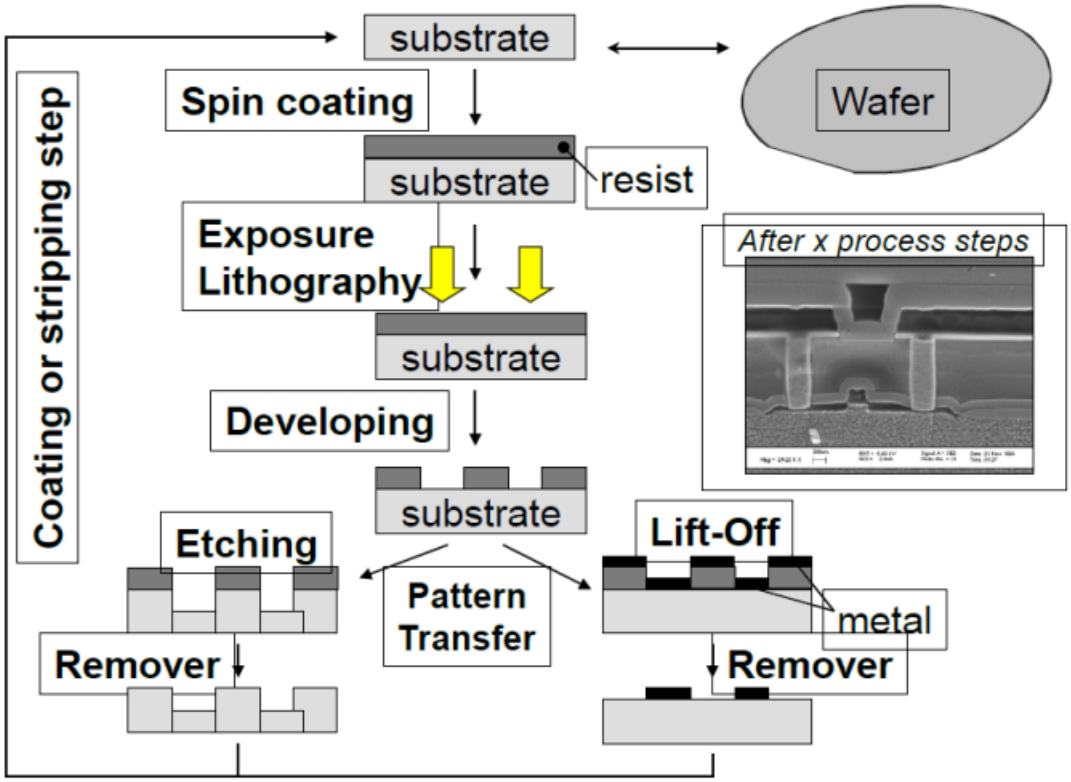


**Figure 4.1.** Diagram for the process flow of the fabrication process of the hybrid waveguide.

Firstly, we will describe the fabrication process for the Si waveguide. We will start from a 220-nm-thick crystalline Si wafer that is placed on top of a 3-µm-thick $SiO_2$ layer. On top of the Si wafer, a negative resist will be deposited by *spin coating*. Next, the mask design contained in the GDS file (see section 4.2) will be drawn in the resist using e-beam laser (exposure lithography). The e-beam changes the properties of the resist in the zones it is applied, and the rest of the resist is removed in the developing process. Since a negative resist was used, it will only be applied the

e-beam in the places that will not be developed. An etching process is then needed to attack the non-resist zones and reveal the mask. Lastly, the remaining resist will be removed to have the Si waveguide.

On the other hand, the process of depositing the $VO_2$ layer is very similar to this previous one. In this case, a positive resist is used. Then, after the developing process, only the zones with resist that has been applied the e-beam will be removed, as opposite to the last case where negative resist was used. This will reveal the zones where the $VO_X$ will be deposited by a molecular beam epitaxy (MBE). Then, the remaining resist is removed, and a lift-off process will be carried out to have only $VO_X$ in the desired regions. Lastly, an annealing process is needed to turn the $VO_X$ into $VO_2$.

## 4.2 Mask design of testing devices

In order to create the testing device, it is needed to design the mask that will be applied to the materials to perform the lithography processes. We will create this mask using a Graphic Design System (GDS) file. These files are the standard in the industry to exchange information on the integrated circuits layout. Within the several available programs to create GDS files, we will be working with KLayout, a popular free software that allows to view and create your own masks.

KLayout will be using a library of structures imported from MATLAB. The main structures we will use to create the mask are focusing gratings, straight waveguides, tapered waveguides and a circle. These building blocks can be seen in the upcoming Fig. 4.2:

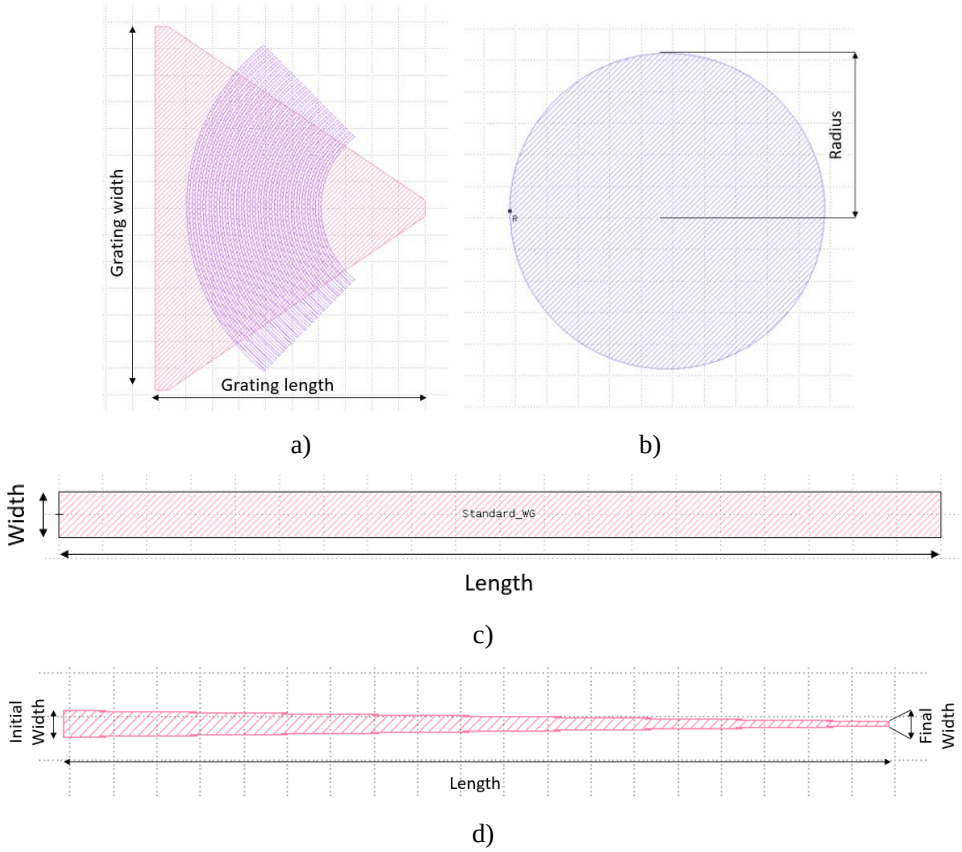


**Figure 4.2.** Building blocks used to create the mask and their dimensions: a) Focusing grating coupler. b) $VO_2$ disc. c) Straight waveguide. d) Tapered waveguide.

Making use of these building blocks, the resultant mask that has been designed and generated in the GDS file is shown in Fig. 4.3. It consists of two grating couplers at both sides in which the optical fibers will be used for coupling light into/out the chip. From left to right, a 3-µm-wide straight waveguide connects to a tapered waveguide which width varies from 3 µm to 0.5 µm. The tapered waveguide is connected to a standard 0.5-µm-wide waveguide that presents a 1-µm radius circle on its centre, which will be the $VO_2$ patch. Then, the mask is symmetrically mirrored. The lengths of every waveguide used are displayed in Fig. 4.3.

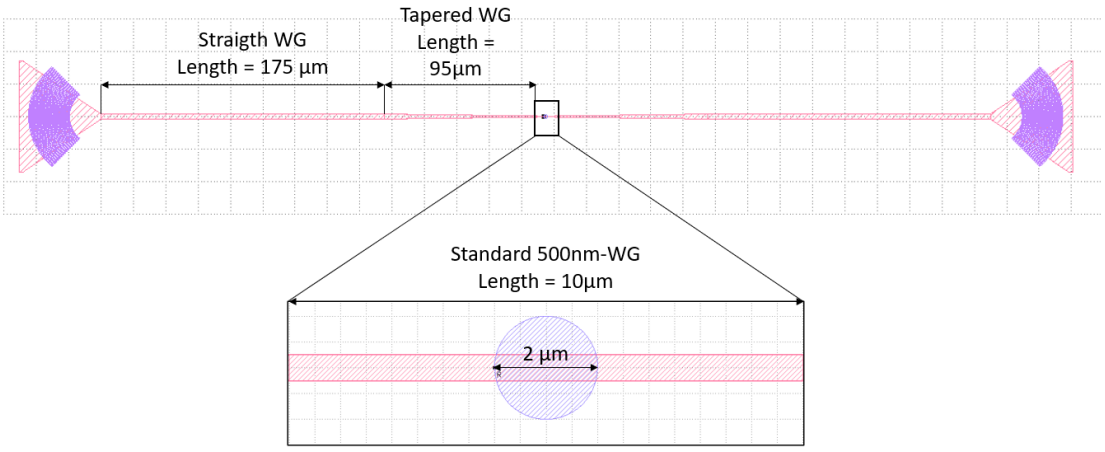


**Figure 4.3.** Final design and dimensions of the mask in the GDS file.

On the other hand, the heater has also been included in the GDS design, although it will not be studied in the preliminary characterization. It consists of a Ti layer that is connected to two aluminium (Al) pads. The electrical current will be injected into these pads, and it will produce thermal energy in the Ti heater (see Fig. 4.4).

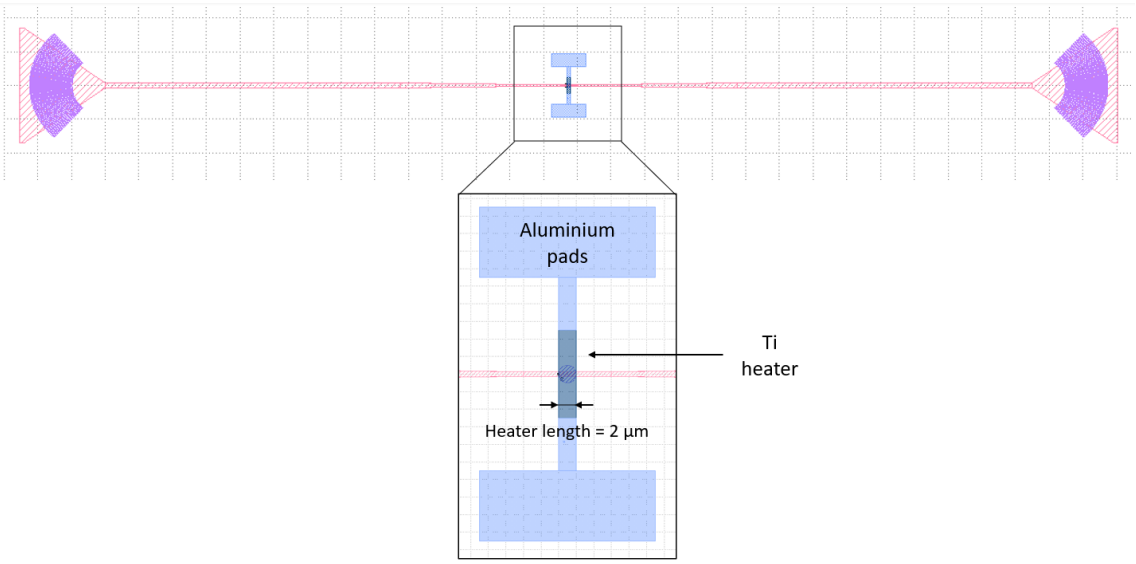


**Figure 4.4.** Final design and dimensions of the mask with the Ti heater and Al pads.

## 4.3 Description of experimental set-up

The setup used to carry out the experimental measurements is described in Figs. 4.5 and 4.6:

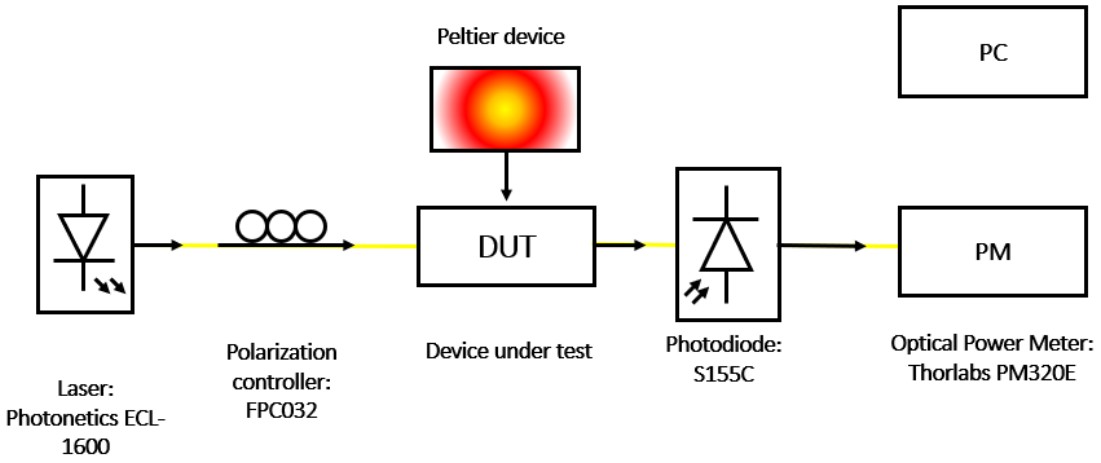


**Figure 4.5.** Schematic of the set-up used for the experimental measurements.

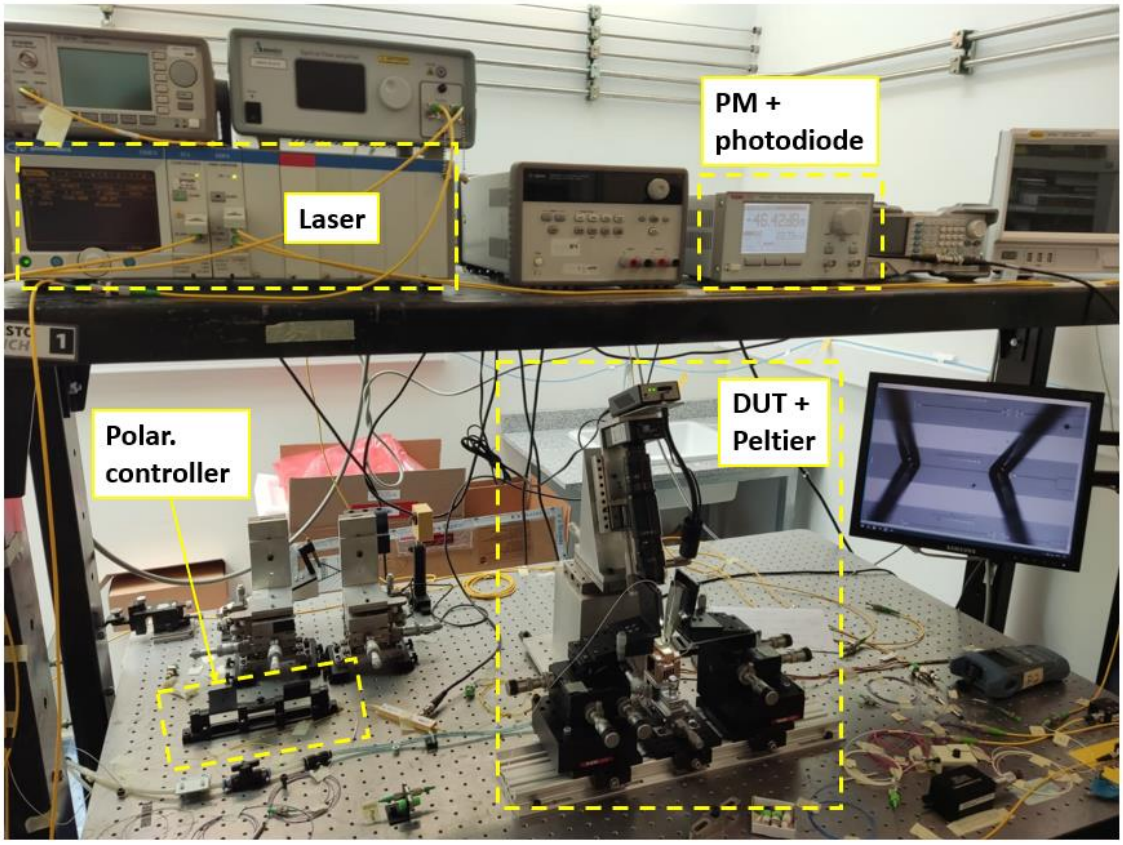


**Figure 4.6.** Set-up used for the experimental measurements.

The laser device inserts a continuous wave (CW) signal with a tunable wavelength that can vary within the range of 1540 to 1640 nm. The injected electrical power is 1 mW (0 dBm).

Next, the polarization controller allows the user to select the polarization of the inserted light. It is formed by three paddles that can rotate around the axis where light is propagated. We will use them to achieve the TM polarization for which the hybrid waveguide is optimized. The paddles must be rotated to attain the maximal power in the output (Power Meter, PM) before performing the measurements. The Device Under Test (DUT) is the photonic chip with gratings where the optical fibers are coupled to insert the light. These gratings have also been optimized for TM polarization.

Besides, the DUT is placed on the holder, which maintains it in position using an air suction mechanism. The optical fibers are adjusted to the coupling graters by means of two positioners that can be moved in the three X, Y, Z dimensions with fine or coarse adjustment. These positioners, as well, are inserted in a rail system that allows to move them sideways. Also, a camera that is connected to a monitor (see Fig. 4.7) will allow us to perform the necessary movements in these positioners to achieve the coupling.

Lastly, a Peltier device is placed under the DUT in order to heat the sample of $VO_2$ and attain the IMT and MIT (see Fig. 4.8). Besides, there is a thermistor on top of the DUT holder. Reading the value of the resistance of the thermistor, we can know what is the temperature at which it is heated. The Peltier is controlled using a thermos-electric controller using the values given by the thermistor. When the temperature is varied, the output power will be shown at the power meter in dBm and the data will be collected and processed using the lab PC.

All the devices (laser, polarization controller, DUT, photodiode and PM) are connected by single-mode optical fiber.

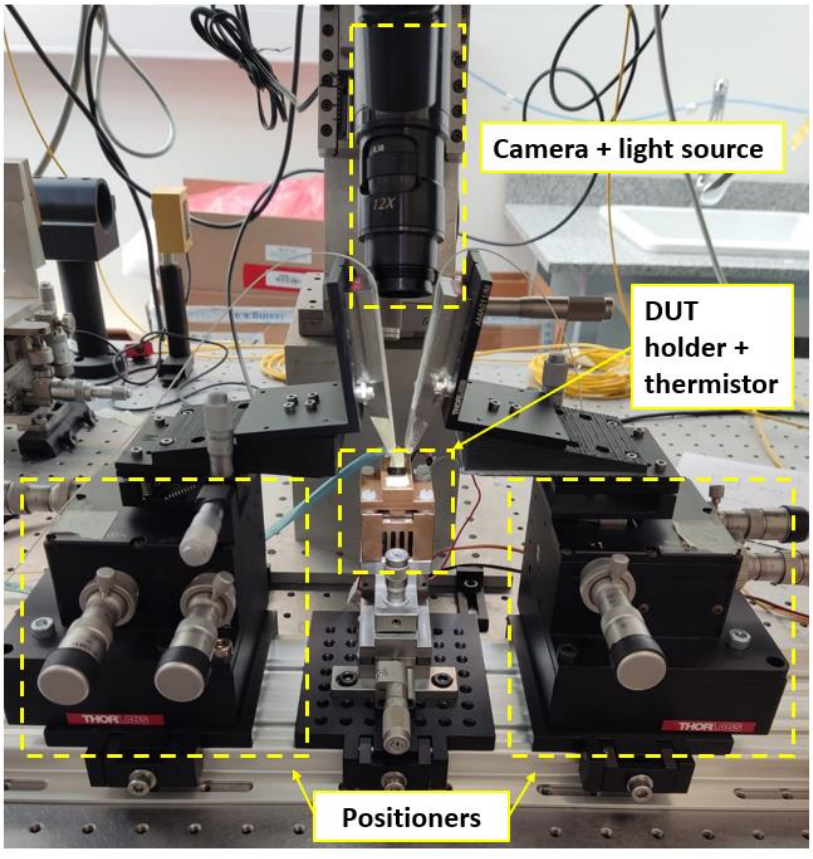


**Figure 4.7.** Zoom-in of the set-up showing the DUT holder, positioners and camera.

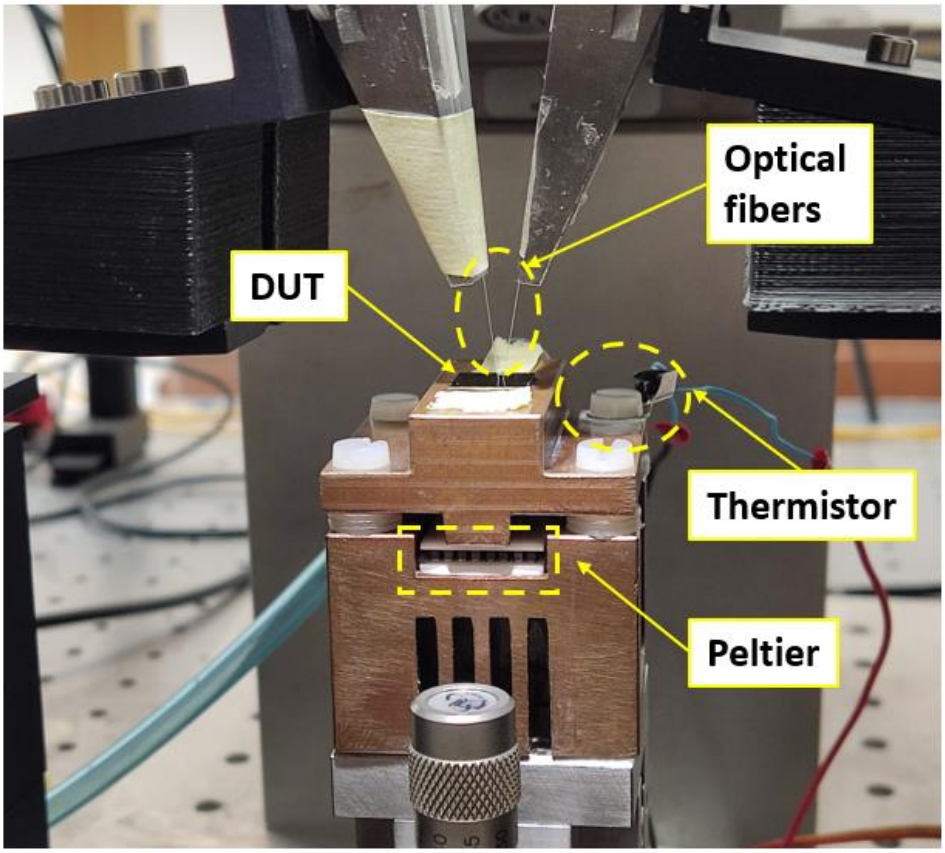


**Figure 4.8.** Zoom-in of the DUT holder showing the optical fibers, the DUT, the thermistor, and the Peltier device.

## 4.4 Experimental results

Once the set-up has been defined and the sample has been fabricated, we will measure the 2-um-long hybrid waveguide performance in the laboratory. The Peltier device located underneath the sample will be heated from 20ºC to 80ºC, and then, back to 20ºC again, with a step of 5ºC between measurements. The temperature variation in the $VO_2$ can be seen in Fig. 4.9:

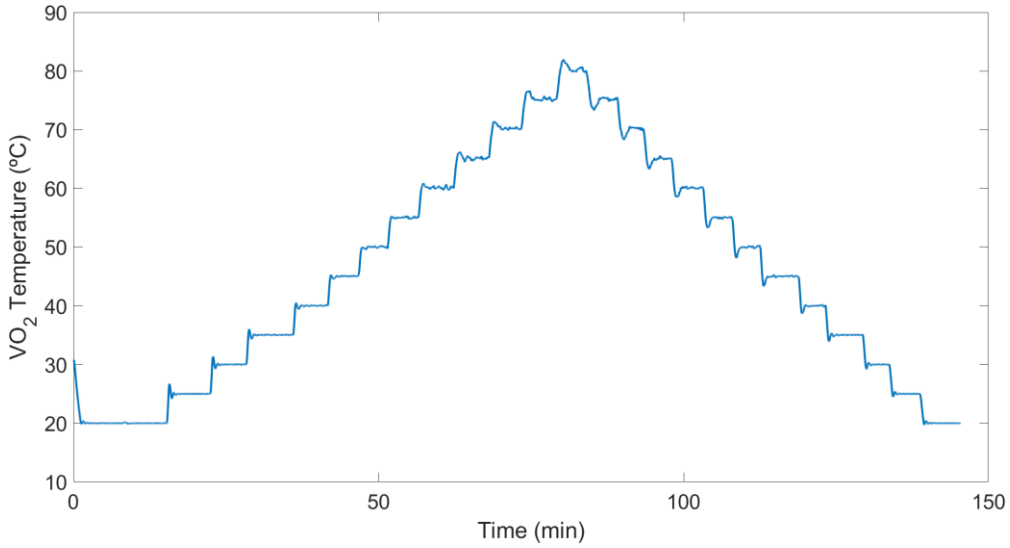


**Fig. 4.9.** $VO_2$ temperature variation across time.

With this variation, we are able to see how the hysteresis process unfolds for λ = 1550 nm (see Fig. 4.10). It can be easily seen that a high-loss state (m-$VO_2$) is achieved when the temperature in the $VO_2$ patch rises to about 60ºC, while, on the contrary, the low-loss state (i-$VO_2$) is not recovered in the cooling process until the $VO_2$ temperature decreases to around 35-40ºC.

The simulation results shown in section 1.1.2 (see Fig. 1.3), which we assumed for working during the entire project, stated that the IMT temperature was around 65ºC, while the MIT temperature was 40ºC. These slight deviations with the experimental results can be attributed to the distance between the thermistor and the actual sample being measured in the laboratory. Since we are measuring the temperature in the thermistor, the temperature in the $VO_2$ layer might actually be higher due to the temperature gradient.

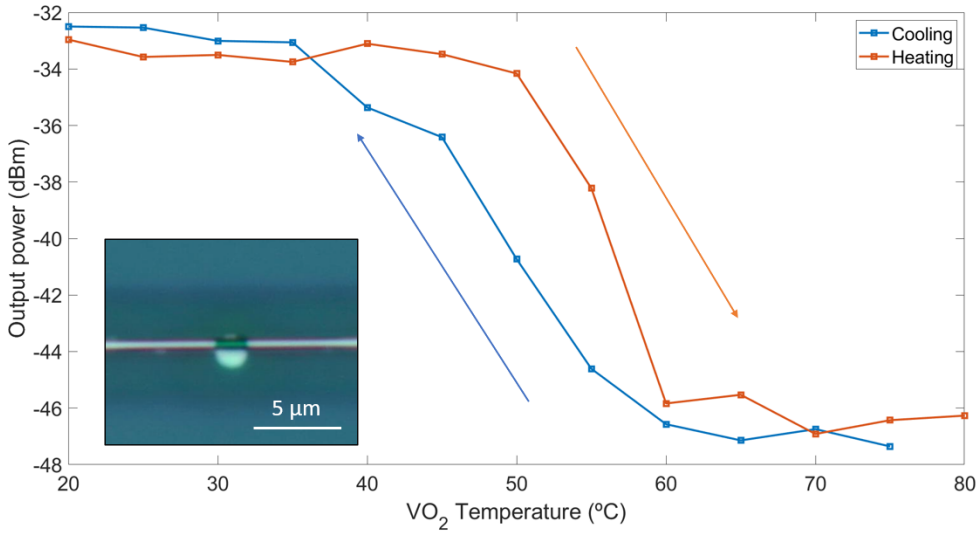


**Fig. 4.10.** Output power (dBm) depending on the $VO_2$ temperature and the heating-cooling process for the 2-µm-long hybrid waveguide and λ = 1550 nm. In-set: microscope image of the 2-µm-long hybrid waveguide.

The next step in the analysis of the experimental results is to study the variation of the waveguide losses with the $VO_2$ temperature, across the C-band wavelengths. We will study this variation in both the heating and the cooling processes (see Fig. 4.11).

It can be seen that the device performs very similarly in both cases, achieving an extinction ratio of about ER = 10 dB for almost all the C-band spectrum. However, the ER decreases in both cases for wavelengths close to λ = 1560 nm. In section 2.4.2, the FullWAVE simulations shown an expected ER = 8.9 dB for a 1.86-μm-long hybrid waveguide (λ = 1550 nm), which these experimental results have confirmed with a moderate accuracy.

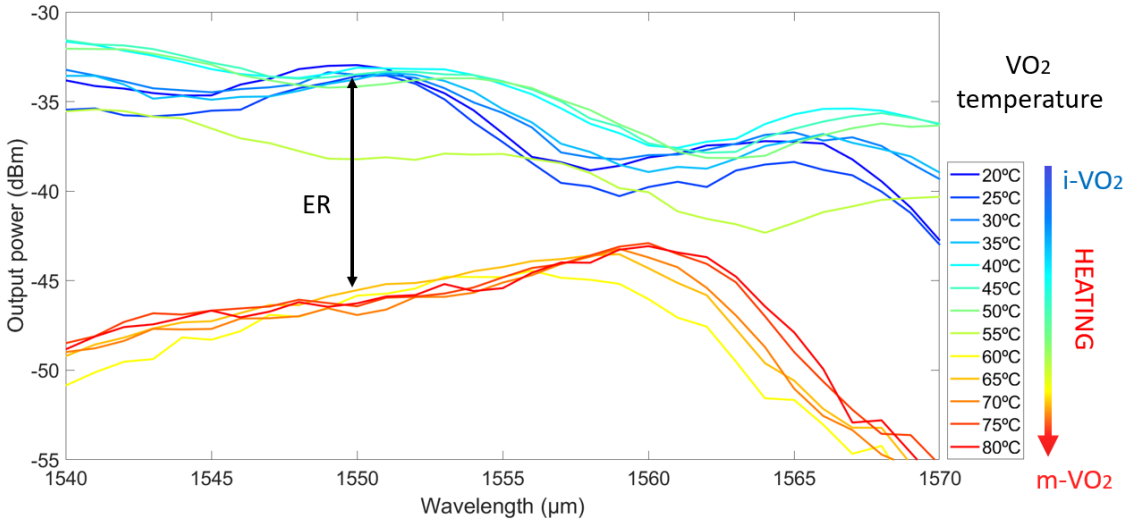


a)

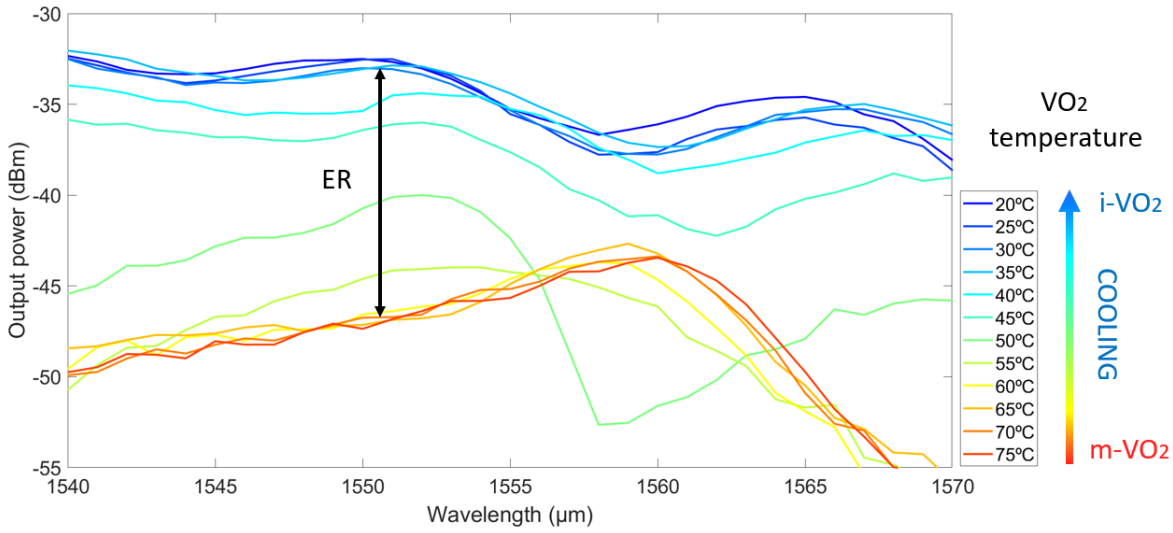


b)

**Figure 4.11.** Output power (dBm) in the 2-μm-long hybrid waveguide across the C-band depending on the temperature. The extinction ratio is intuitively depicted as the difference of losses between the lowest and highest $VO_2$ temperatures. a) Heating process. b) Cooling process.

# Chapter 5. Conclusions and future work

## 5.1 Conclusions

As it was stated in the introduction to this project, the increase in data consumption that has taken place in the last years has revealed a need for faster and more efficient data processing. In this context, photonics could be taking a leading role in the next generation of computing devices. In this project, we have addressed this subject from the point of view of silicon photonics and phase-change materials (PCMs). More specifically, a hybrid $VO_2$/Si waveguide with $SiO_2$ cladding has been developed, with the prospect of being utilized as a building block in photonic neural networks. This hybrid waveguide acts as an optical switch triggered by thermal stimulation, achieving the transition from i-$VO_2$ (low losses) to m-$VO_2$ (high losses) (IMT) at around 65ºC. It has also been designed for C-band telecommunications ($\lambda$ = 1530 – 1565 nm).

In order to design this hybrid waveguide, a standard 220x500 nm Si waveguide was selected. Then, a $VO_2$ patch was placed on top of this waveguide. The first milestone in this project was to achieve the optimal dimensions for this $VO_2$ patch so as to minimize the total losses. After a series of numerical simulations (assuming $\lambda$ = 1550 nm) using RSoft software, we concluded that the optimal $VO_2$ thickness was 40 nm, with a length of 1.86 μm for an ER of 10 dB, and 3.72 μm for an ER of 20 dB. In all cases, we established that the polarization used would be TM, since it gave place to higher ER using lower lengths, therefore resulting in more compact hybrid waveguides.

The next step in the development of the device was to determine the optimal distance between the $VO_2$ and the heater used for switching the state of the hybrid $VO_2$/Si waveguide. A Ti heater was utilized for this purpose. Heat arises when an electrical current is injected to the Ti due to Joule effect. Since Ti is an optically non-transparent material, it could generate additional losses in the device. For that matter, it was necessary to place the Ti heater at a certain distance from the waveguide. By means of optical and thermal transmission simulations, using RSoft and COMSOL software, we obtained that the minimal gap distance at which the Ti heater could be placed is 0.8 μm apart from the hybrid waveguide. For this value, we also obtained that the minimal power that needed to be injected in the heater was 0.994 mW. The minimal switching time for this heating configuration was as fast as 29.85 μs.

Lastly, and once the hybrid waveguide optimal dimensions and its heater configuration were obtained, a preliminary experimental characterization of the device was carried out in the laboratory for $\lambda$ = 1540 – 1570 nm to characterize the optical performance of the device. For this experiment, the analysed hybrid waveguide lacked the Ti heater and the $SiO_2$ cladding. To control the phase change of the $VO_2$, a Peltier device was used. The IMT temperature was proven to be at around 60ºC. Finally, and most importantly, the 2-μm-long $VO_2$/Si hybrid waveguide was demonstrated to perform satisfactorily, achieving, as expected, an ER of around 10 dB for the whole C-band spectrum.

## 5.2 Future work

Next steps would be to complete the fabrication of the device by depositing the $SiO_2$ with the optimal thickness and the Ti heater. In this regard, power consumption and switching time would be characterized. Furthermore, it would also be possible to carry out an experimental measurement of the performance of the hybrid waveguide using the designed Ti heater. In this project, a Peltier device was used in the laboratory to heat the $VO_2$ and achieve the IMT. Thus, analysing the real performance of the complete design (Ti microheater included) would be a very interesting line of work for the future.

Besides, another topic to discuss would be the heater material. Optically transparent materials such as transparent conducting oxides (TCOs), e.g., indium tin oxide (ITO) would induce much lower losses, eliminating the need for a gap between the heater and the hybrid waveguide. This way, the needed injected power, as well as the switching times would be drastically reduced, yielding a more efficient device [23], [24].

Lastly, future work would also include studying the performance of the hybrid waveguide for TE polarization. In section 2.3.3, a comparison between both polarizations has been exhibited. We selected the TM fundamental mode because it had a better performance than TE when only the $VO_2$ top layer underwent IMT. Nonetheless, TE polarization performs better than TM in the case that the IMT takes place in all the $VO_2$ layers. Because of this, a new line of study for this project would be to analyse this situation.

# Chapter 6. References

[1] Q. Cheng, S. Rumley, M. Bahadori, and K. Bergman, "Photonic switching in high performance datacenters [Invited]," *Opt Express*, vol. 26, no. 12, pp. 16022–16043, 2018, doi: 10.1364/OE.26.016022.

[2] G. Kamiya, "Data Centres and Data Transmission Networks," *IEA*, Jun. 29, 2023.

[3] A. H. Atabaki *et al.*, "Integrating photonics with silicon nanoelectronics for the next generation of systems on a chip," *Nature*, vol. 556, no. 7701, pp. 349–354, Apr. 2018, doi: 10.1038/s41586-018-0028-z.

[4] M. Wuttig and N. Yamada, "Phase-change materials for rewriteable data storage," *Nat Mater*, vol. 6, no. 11, pp. 824–832, Nov. 2007, doi: 10.1038/nmat2009.

[5] Y. Ke, S. Wang, G. Liu, M. Li, T. J. White, and Y. Long, "Vanadium Dioxide: The Multistimuli Responsive Material and Its Applications," *Small*, vol. 14, no. 39, p. 1802025, Sep. 2018, doi: 10.1002/smll.201802025.

[6] Z. Yang, C. Ko, and S. Ramanathan, "Oxide Electronics Utilizing Ultrafast Metal-Insulator Transitions," *Annu Rev Mater Res*, vol. 41, no. 1, pp. 337–367, Aug. 2011, doi: 10.1146/annurev-matsci-062910-100347.

[7] N. Youngblood, C. A. Ríos Ocampo, W. H. P. Pernice, and H. Bhaskaran, "Integrated optical memristors," *Nat Photonics*, May 2023, doi: 10.1038/s41566-023-01217-w.

[8] J. Parra, T. Ivanova, M. Menghini, P. Homm, J.-P. Locquet, and P. Sanchis, "All-Optical Hybrid VO2/Si Waveguide Absorption Switch at Telecommunication Wavelengths," *Journal of Lightwave Technology*, vol. 39, no. 9, pp. 2888–2894, May 2021, doi: 10.1109/JLT.2021.3054942.

[9] J. He, T. Dong, and Y. Xu, "Review of Photonic Integrated Optical Phased Arrays for Space Optical Communication," *IEEE Access*, vol. 8, pp. 188284–188298, 2020, doi: 10.1109/ACCESS.2020.3030627.

[10] X. Sun, L. Zhang, Q. Zhang, and W. Zhang, "Si Photonics for Practical LiDAR Solutions," *Applied Sciences*, vol. 9, no. 20, p. 4225, Oct. 2019, doi: 10.3390/app9204225.

[11] J. Lederer, "Activation Functions in Artificial Neural Networks: A Systematic Overview," Jan. 2021.

[12] B. J. Shastri *et al.*, "Photonics for artificial intelligence and neuromorphic computing," *Nat Photonics*, vol. 15, no. 2, pp. 102–114, Feb. 2021, doi: 10.1038/s41566-020-00754-y.

[13] S. Cueff *et al.*, "VO2 nanophotonics," *APL Photonics*, vol. 5, no. 11, Nov. 2020, doi: 10.1063/5.0028093.

[14] J. Parra, J. Navarro-Arenas, M. Menghini, M. Recaman, J. Pierre-Locquet, and P. Sanchis, "Low-threshold power and tunable integrated optical limiter based on an ultracompact VO2/Si waveguide," *APL Photonics*, vol. 6, no. 12, Dec. 2021, doi: 10.1063/5.0071395.

[15] J. Kischkat *et al.*, "Mid-infrared optical properties of thin films of aluminum oxide, titanium dioxide, silicon dioxide, aluminum nitride, and silicon nitride," *Appl Opt*, vol. 51, no. 28, p. 6789, Oct. 2012, doi: 10.1364/AO.51.006789.

[16] H. H. Li, "Refractive index of silicon and germanium and its wavelength and temperature derivatives," *J Phys Chem Ref Data*, vol. 9, no. 3, pp. 561–658, Jul. 1980, doi: 10.1063/1.555624.

[17] P. Johnson and R. Christy, "Optical constants of transition metals: Ti, V, Cr, Mn, Fe, Co, Ni, and Pd," *Phys Rev B*, vol. 9, no. 12, pp. 5056–5070, Jun. 1974, doi: 10.1103/PhysRevB.9.5056.

[18] A. H. Atabaki, E. Shah Hosseini, A. A. Eftekhar, S. Yegnanarayanan, and A. Adibi, "Optimization of metallic microheaters for high-speed reconfigurable silicon photonics," *Opt Express*, vol. 18, no. 17, p. 18312, Aug. 2010, doi: 10.1364/OE.18.018312.

[19] "The Engineering ToolBox - Thermal Conductivity of Metals," Jun. 29, 2023.

[20] "The Engineering ToolBox - Metals and Alloys, Densities," Jun. 29, 2023.

[21] "The Engineering ToolBox - Specific Heat of Common Substances," Jun. 29, 2023.

[22] M. Sadeghi, B. Janjan, M. Heidari, and D. Abbott, "Mid-infrared hybrid Si/$VO_2$ modulator electrically driven by graphene electrodes," *Opt Express*, vol. 28, no. 7, p. 9198, Mar. 2020, doi: 10.1364/OE.381948.

[23] H. Taghinejad *et al.*, "ITO-based microheaters for reversible multi-stage switching of phase-change materials: towards miniaturized beyond-binary reconfigurable integrated photonics," *Opt Express*, vol. 29, no. 13, p. 20449, Jun. 2021, doi: 10.1364/OE.424676.

[24] J. Parra, J. Hurtado, A. Griol, and P. Sanchis, "Ultra-low loss hybrid ITO/Si thermo-optic phase shifter with optimized power consumption," *Opt Express*, vol. 28, no. 7, p. 9393, Mar. 2020, doi: 10.1364/OE.386959.